Angular-resolved ultraviolet photoemission spectroscopy and its application to the layer compounds $TaSe_2$ and TaS_2

N. V. Smith and M. M. Traum
Bell Laboratories, Murray Hill, New Jersey 07974
(Received 17 September 1974)

Photoelectron energy spectra have been measured on the layer compounds $1T$-$TaSe_2$, $1T$-TaS_2, and $2H$-$TaSe_2$ as a function of both polar and azimuthal angle of emission. Light was incident normally upon the sample and the photon energy in most of the experiments was 10.2 eV. The measurements were performed in a specially constructed ultrahigh vacuum chamber using a movable retarding potential-energy analyzer. The variations with polar angle of the positions of peaks in the spectra have been used to plot experimental energy bands which are found to compare favorably with the first-principles calculations of Mattheiss. The azimuthal dependence of the photoemission, and in particular the Ta d-emission intensity, was found to display strong anisotropies. X-ray orientation of the $1T$ samples revealed that if one assumes that the Ta d photoelectrons originate on Ta atoms, then they propagate preferentially along directions which avoid neighboring chalcogen atoms. The relationship with atomic orbitals and band theory is discussed. In the hexagonal crystal $2H$-$TaSe_2$, residual threefold rotational symmetry is observed in the Ta d emission and is attributed to the shortness of the photoelectron escape depth.

I. INTRODUCTION

It has been recognized for some time[1] that it would be desirable to measure the photoelectron energy spectra of solids as a function of the angle of emission. So far, relatively few experiments of this kind have been performed.[2-16] A conventional photoemission experiment integrates the emission over a large solid angle, and, in many cases, over the entire solid angle into which the emission occurs. Our original motivation for such angular studies was a desire to map energy–versus–wave-vector dispersion relations for electronic states in solids directly from experiment. This first aim was finally achieved on the layer materials $1T$-$TaSe_2$ and $1T$-TaS_2, and a preliminary account of this work has appeared elsewhere.[15] During the course of the work it emerged that the technique was capable of providing information not only on the energy bands but also on the electronic wave functions.[14] This follows if one turns one's attention to peak intensities rather than peak positions. Peak positions are determined largely by the energy bands (i.e., the energy eigenvalues of the electron Hamiltonian). Peak intensities, on the other hand, depend on the momentum matrix elements of the optical transitions and therefore on the electron wave functions.

The way in which angular photoemission studies should reveal the energy bands is readily understood as follows. Let us suppose that we have measured the kinetic energy E of an electron photoemitted into vacuum, and that we have also determined θ and ϕ, the angles of propagation of the electron. The polar angle θ is defined here as the angle between the electron's trajectory and the outward normal to the surface of the photoemitting sample. The azimuthal angle ϕ represents the angle of rotation about the normal. Measurements of E, θ, and ϕ yield values for the three components of the electron's wave vector, $\vec{k}'$, in vacuum. Taking the z axis along the surface normal, we have simply:

$$k'_x = (2mE/\hbar^2)^{1/2}\sin\theta\cos\phi,$$
$$k'_y = (2mE/\hbar^2)^{1/2}\sin\theta\sin\phi, \quad (1)$$
$$k'_z = (2mE/\hbar^2)^{1/2}\cos\theta.$$

These components may be related to the components k_x, k_y, and k_z of the wave vector $\vec{k}$ which the electron had inside the material. If the refraction of the electron wave on crossing the surface boundary is specular, the components parallel to the surface, k_x and k_y, will be conserved. The perpendicular component k_z presents more of a problem. In a simple free-electron picture, the perpendicular component k_z will be given by

$$\frac{\hbar^2 k_z^2}{2m} = \frac{\hbar^2 k_z'^2}{2m} + W, \quad (2)$$

where W is the inner potential. We have attempted to apply this free-electron refraction condition in the analysis of our first angular photoemission studies which were performed on GaAs.[13] The uncertainties involved in the use of a free-electron refraction condition in a material such as GaAs, having a complicated band structure, led us to conclude that further interpretation along these lines would not be fruitful at this stage. We turned our

attention instead to two-dimensional materials.

The problems indicated above are alleviated in layer compounds such as the transition-metal dichalcogenides (TX_2). These materials consist of covalently bonded X-T-X sandwiches which are loosely coupled to one another by van der Waals interactions.[17] Since electrons tend to be localized within individual sandwiches, the energy bands in the direction perpendicular to the sandwiches are expected to be rather flat. Therefore, the band structure is almost completely specified once it is known in the two dimensions parallel to the crystal layers. The validity of this assumption will be discussed in Sec. II below from the vantage point of recent first-principles band calculations by Mattheiss.[18] If the assumption of flatness is correct, however, it means that in angular photoemission studies of layer compounds, we need not concern ourselves with the k_z dependence but can concentrate on the k_x and k_y dependence of the spectra and the energy bands. Angular-resolved photoemission measurements have been made previously as a function of θ on the layer compound MoS_2 by Williams *et al.*,[9] and an analysis of their results has been presented by Hughes and Liang.[19] Conventional photoemission work on various layer transition-metal dichalcogenides has been done in a number of other laboratories.[20–24]

After describing in Sec. III the details of our experimental method, we present in Sec. IV results for the polar-angle dependence of the photoelectron energy spectra in $1T$-$TaSe_2$, $1T$-TaS_2, and $2H$-$TaSe_2$. From the positions of peaks in these spectra, we map the two-dimensional energy bands in the manner outlined above. These experimental energy bands are compared with the first-principles calculations of Mattheiss.

In Sec. V we present results for the dependence of the spectra on azimuthal angle. The emphasis here will be on variations of the peak intensities rather than the peak positions. We shall concentrate in particular on the intensity of emission from the Ta-derived d states. The results will be discussed from two points of view, one which places its emphasis on the properties of the final states in the optical transitions, and another which places its emphasis on the role of the initial states. An important part of our discussion will be concerned with the requirements of threefold as opposed to sixfold rotational symmetry in the azimuthal dependence of the Ta d emission. In the $1T$ materials, for example, a strict adherence to the two-dimensional assumption requires that the energy bands have sixfold rotational symmetry. On the other hand, the site symmetry of the Ta atoms and the Ta-derived d wave functions maintains threefold symmetry. In $2H$-$TaSe_2$, which has a hexagonal crystal structure, it will be argued that the observation of residual threefold symmetry is a surface effect due to the smallness of the photoelectron attenuation length.

II. PROPERTIES OF LAYER COMPOUNDS

We review here those properties of layer compounds which we will need below in Secs. IV and V in the interpretation of our experimental photoemission results. We describe first the crystal structures of the $1T$ and $2H$ polytypes. We discuss also the electronic energy bands for the $1T$ and $2H$ polytypes of TaS_2.

A. Crystal structure

An interesting and useful property of layer compounds such as the transition metal dichalcogenides is that the same compound can often be prepared with different crystal structures. These different structures, or polytypes, share in common the X-T-X sandwich sequence of the atomic layers. They differ, however, in the coordination of the T atoms, and also in the stacking and registry of successive sandwiches with respect to each other. In $TaSe_2$, for example, the following polytypes have been identified[25]: $1T$, $2H$, $3R$, $4Ha$, $4Hb$, $4Hc$, and $6H$. In our work, we have investigated only the two simplest structures, namely the $1T$ and $2H$ polytypes.[26] Their unit cells are illustrated in Fig. 1.

In the $1T$ structure (space group D_{3d}^3), each T atom is octahedrally coordinated with X atoms. Only one sandwich is required to define the unit cell in the c direction, and the structure has trigonal symmetry about the c axis: hence the designation "$1T$." To be more precise, the coordination is not quite octahedral, but, due to distortion along the c axis, is actually trigonal antiprismatic. Another refinement concerns the positional parameter

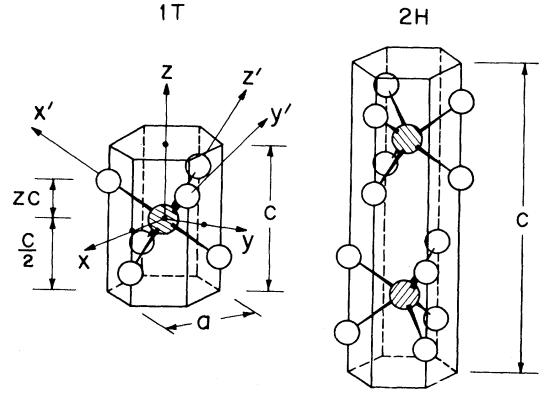

FIG. 1. Unit cells of the crystal structures of the $1T$ and $2H$ polytypes of the layer transition-metal dichalcogenides. Cross-hatched circles represent metal atoms. Open circles represent chalcogen atoms.

z defined in Fig. 1. Bjerkelund and Kjekshus[27] find for $1T$-$TaSe_2$ a value of z equal to 0.25 ± 0.01, a range which contains the "ideal" value of $\frac{1}{4}$. Our own x-ray diffraction studies described in Sec. III D suggest a value somewhat greater than 0.25. We indicate in the $1T$ unit cell of Fig. 1 the directions of the x, y, z axes. Also shown are an alternative set of axes x', y', z' which will prove convenient in Sec. V when we discuss crystal-field splittings in an octahedral ligand field.

In the $2H$ polytype (space group D_{6h}^4), the coordination of the T atoms is trigonal prismatic. The unit cell in the c direction spans two sandwiches, and the crystal point group is hexagonal, hence the "$2H$" designation. As can be seen from Fig. 1 each individual X-T-X sandwich has threefold rotational symmetry about the c axis. The orientations of alternate sandwiches are separated by a 180° rotation about the c axis. In other words, the sixfold symmetry operation involves not only a 60° rotation, but also a nonprimitive translation parallel to the c axis. Introduction of a surface into the problem will break translational symmetry parallel to the c axis. Since the sixfold symmetry involves such a translation, it also will be broken and there will be a reversion to the lower threefold rotational symmetry. This lower symmetry has been observed in the photoemission properties of $2H$-$TaSe_2$. These results have been reported elsewhere,[16] and will be discussed further in Sec. V F.

An effect not considered in detail in this paper is the occurrence of superlattice formation in the crystal structures of the room-temperature phase in $1T$-$TaSe_2$ and $1T$-TaS_2.[17,28,29] The superlattices are thought to come about through the locking in of the crystal structure to the periodicity of a charge density wave associated with certain regions of the Fermi surface.[29] In the new crystal structure the lattice parameter a is $\sqrt{13}$ times larger than that indicated in Fig. 1, with the new unit cell being nearly hexagonal but rotated by ~13° about the c axis. However, the displacements of the atoms from the $1T$ positions are less than 0.1 Å, a value comparable to the root-mean-square thermal displacements at room temperature. Within the finite angular resolution of our experimental apparatus, the superlattice structure cannot be distinguished from the perfect $1T$ structure. We have assumed, therefore, that superlattice effects are not likely to be important in the interpretation of our photoemission results. Possible exceptions to this will be mentioned briefly in Sec. V E.

B. Electronic structure

Band schemes for transition metal dichalcogenides have been presented by a number of authors.[17,30-37] First-principles band structures for $1T$-TaS_2 and $2H$-TaS_2 calculated recently by Mattheiss[18] using the augmented plane wave (APW) method are shown in Figs. 2 and 3, respectively. In the energy range -0.13 to 0.22 Ry, there exists, in both polytypes, a group of bands which are derived primarily from the S $3p$ orbitals. At slightly higher energies lie the Ta-derived $5d$ bands. The dashed bands in the upper portions of Figs. 2 and 3 correspond to the Ta-derived $6s$, $6p$ bands.

In the octahedrally coordinated material $1T$-TaS_2, the fivefold $5d$ band is split into two nonoverlapping subbands. The threefold lower subband is associated with the $5d$ orbitals, $d_{3z^2-r^2}$, d_{xy}, and $d_{x^2-y^2}$, loosely referred to as the "t_{2g}" orbitals. The twofold upper subband is associated with the "e_g" orbital d_{yz} and d_{zx}. As will be discussed in Sec. V C, these orbitals are not the true t_{2g} and e_g orbitals, but are closely related to them. The main point for our present purposes is that the Fermi energy falls in the lower subband, so that the occupied Ta d orbitals are expected to be primarily of t_{2g} character. The density-of-states calculations by Mattheiss (see Fig. 10 of Ref. 18) indicate that the orbitals $d_{3z^2-r^2}$, d_{xy} and $d_{x^2-y^2}$ are all strongly represented in the occupied region.

In $2H$-TaS_2 there are twice as many bands as in $1T$-TaS_2 because there are twice as many atoms per unit cell. The Ta $5d$ bands are split into an eightfold upper subband and a narrow twofold lower subband. The latter corresponds roughly to the $d_{3z^2-r^2}$ band of earlier empirical band schemes.[17,30,33] However, as shown by Mattheiss, this subband contains a strong admixture of the other "t_{2g}" orbitals, d_{xy} and $d_{x^2-y^2}$. Indeed, the hybridization between the $d_{3z^2-r^2}$ and d_{xy}, $d_{x^2-y^2}$ derived bands is crucial in bringing about the large gap between the twofold and eightfold subbands.

The Brillouin zone of the $1T$ structure is shown in Fig. 4. We discuss here those features of its geometry which will be relevant to further discussion concerning sixfold as opposed to threefold rotational symmetry. The irreducible wedge of the Brillouin zone is indicated by bold lines in Fig. 4, and the symmetry points Γ, A, L, M, H, and K have all been labeled. The points M' and L' in Fig. 4 are fully equivalent by symmetry to M and L, respectively, but have been given primed labels for the following reason. The perimeters of the rectangles ΓALM and $\Gamma AL'M'$ are fully equivalent to each other by symmetry, but the interiors of these rectangles are not. Likewise, the energy bands [$\mathcal{E}(\vec{k})$ dispersion relations] over all corresponding surfaces of the shaded and unshaded wedges in Fig. 4 are equivalent by symmetry, but there is no requirement of crystal symmetry which demands that the $\mathcal{E}(\vec{k})$ relations be identical in the interior of these two kinds of wedge. The Brillouin zone and the energy bands therefore retain the threefold rotational symmetry of the real-space crystal struc-

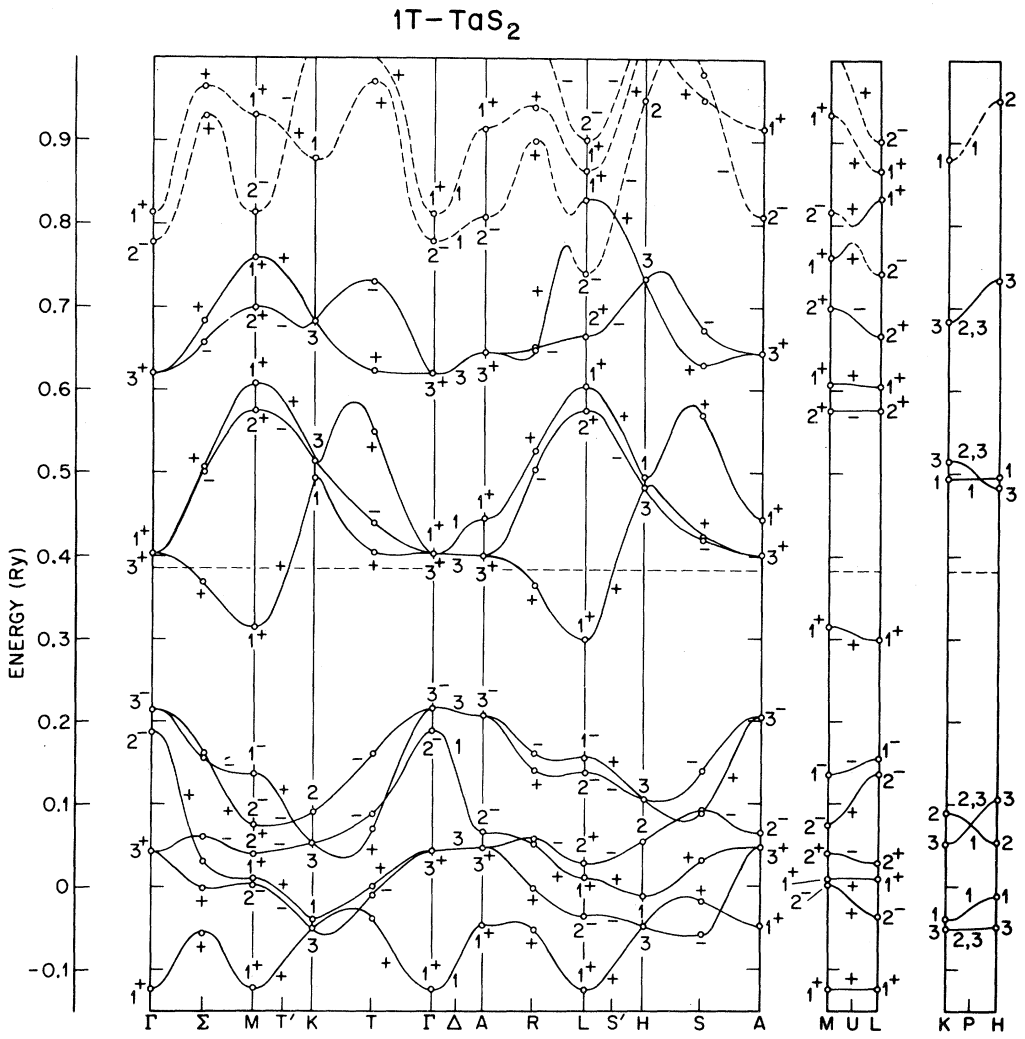

FIG. 2. Energy-band structure of $1T$-TaS_2 (courtesy Mattheiss).

ture. The k_x, k_y, k_z axes of Fig. 4 are parallel respectively to the x, y, z axes of Fig. 1, so that the unshaded wedges of Fig. 4 are the ones which would correspond to the locations of the nearest-neighbor chalcogen atoms if one were to imagine a metal atom placed at the origin of k space.

Since the $\mathcal{E}(\vec{k})$ relations are constrained to be identical over the surfaces of the two kinds of wedge, one expects some tendency for them to be similar in the interiors. This tendency is greatly reinforced if one invokes the approximation of two dimensionality. If the bands were perfectly flat in the k_z direction, the energy bands along ΓM would then be identical with those along AL, and any other direction parallel to ΓM or $\Gamma M'$. Similarly, the $\mathcal{E}(\vec{k})$ dispersion relations would become identical in the shaded and unshaded wedges, and would therefore display full sixfold rotational symmetry.

Inspection of the first-principles energy bands in Fig. 2 for the ΓA, ML and KH directions reveals that there is some justification for the assumption of flatness of the bands along k_z in the occupied region; the few exceptions to this have been discussed by Mattheiss. In summary, therefore, we expect the occupied energy bands in $1T$-TaS_2 (and also $1T$-$TaSe_2$) to have sixfold symmetry or something close thereto. In anticipation of results to be presented in Sec. V, we note that if strong threefold symmetry is observed in the photoemission properties of the $1T$ materials, it appears that we must look beyond the initial-state $\mathcal{E}(\vec{k})$ relations for the explanation.

The Brillouin zone for the $2H$ structure is very similar to that for the $1T$ structure. However, since the crystal has sixfold rotational symmetry, there is no longer any distinction between the shaded

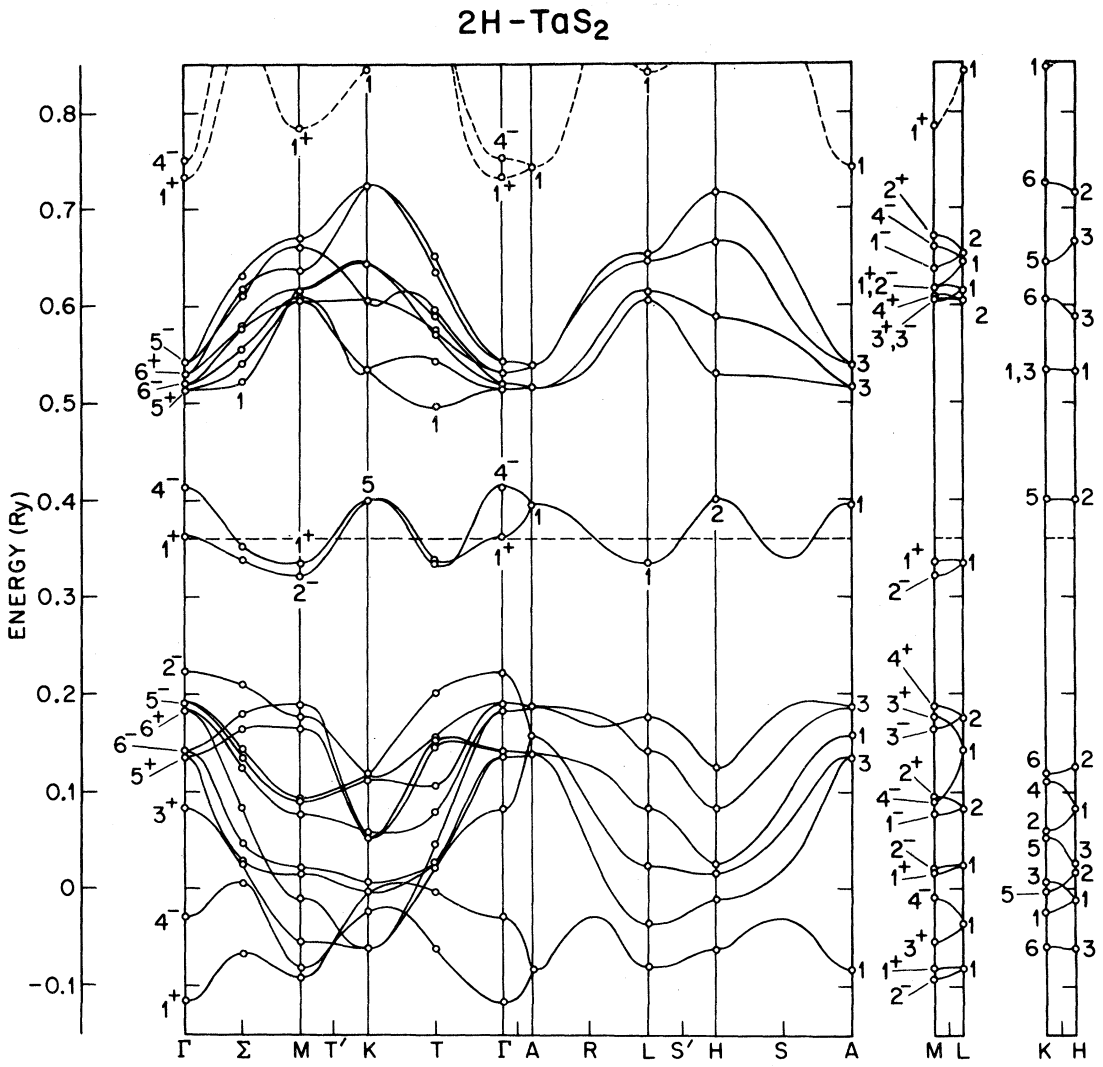

FIG. 3. Energy band structure of $2H$-TaS_2 (courtesy Mattheiss).

and unshaded wedges of Fig. 4. If the photoemission properties of a $2H$ material, therefore, display even weak threefold symmetry, we must look beyond the occupied and unoccupied energy bands for the explanation.

III. EXPERIMENTAL METHOD

A. Chamber and analyzer

A special stainless steel ultrahigh vacuum chamber was built for these angular dependence experiments, and a schematic plan of it is shown in Fig. 5. The positions of the photoelectron energy analyzer and sample are also shown. Ultraviolet light from the exit slits of a McPherson 225 monochromator passes through a LiF window and enters an antechamber where it impinges on an ellipsoidal mirror, which in turn brings the light to a focus on the surface of the sample situated at the center of the main chamber. The mirror was made of stainless steel and was coated with an evaporated film of gold. The sample and the monochromator exit

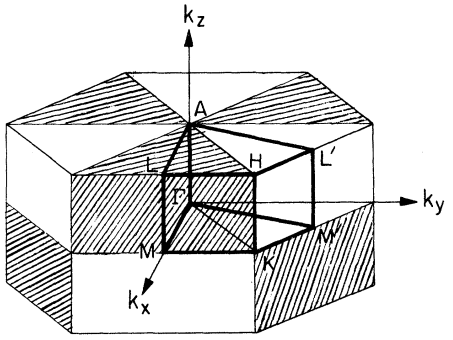

FIG. 4. Brillouin zone of the $1T$ polytype.

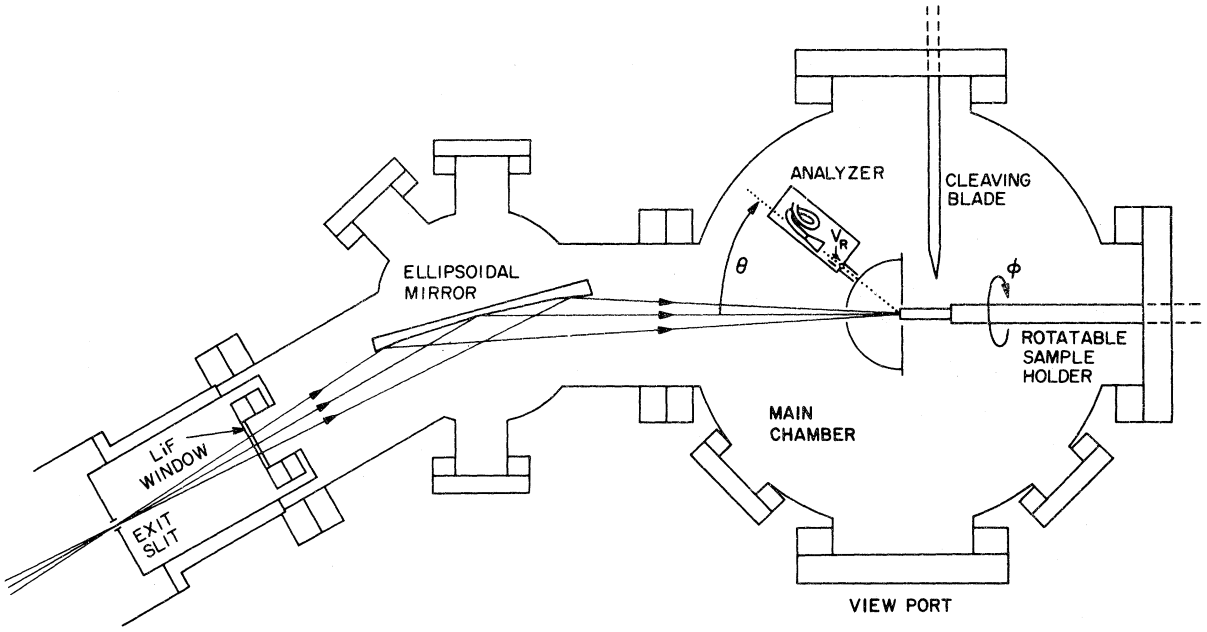

FIG. 5. Schematic plan of the measuring chamber and photoelectron analyzer.

slits sit close to the foci of the ellipsoidal surface of the mirror. In practice, the illuminated spot on the sample was a somewhat enlarged image of the exit slit with linear dimensions of 3–5 mm.

The sample is surrounded by a copper hemispherical shell whose function is to create a drift region free from electrostatic fields. A slot permits photoelectrons propagating in the plane of the figure to exit from the hemisphere into an energy analyzer which, by means of a rotary motion, can be positioned at various polar angles θ with respect to the surface normal. The azimuthal angle ϕ is varied by rotating the sample about its surface normal. To achieve this, the sample was mounted on a Varian 981-0523 precision manipulator which, in addition to the rotary motion, permits the sample to be translated in the longitudinal direction and in two perpendicular transverse directions. These linear motions were used in fine adjustments of the position of the sample and also in the sample-cleaving procedure described below.

The energy analyzer indicated in Fig. 5 was operated on the retarding field principle. In most of our experiments, the entrance tube of the analyzer was kept at the same potential as the hemisphere, thereby extending the field-free region up to the aperture (1.5-mm diam) at the end of the entrance tube (3-mm inner diam). Photoelectrons which pass through the aperture enter a second tube of 3-mm inner diam to which the retarding potential V_R is applied. Those electrons which emerge from the end of the retarding tube are collected by a Bendix 4028 channel electron multiplier. Since the aperture in the analyzer is rather small, the angular resolution is determined partly by the angular size of the illuminated spot on the surface of the sample and partly by the collimating effect of the various apertures through which the electrons must pass. The azimuthal resolution $\Delta\phi$ is estimated to be about 4° (i.e., there is a spread of ±2° on each side of our stated values for ϕ); $\Delta\phi$ is independent of θ or ϕ. The polar resolution $\Delta\theta$ is estimated to be about 4° for small θ, but is expected to decrease with increasing θ due to the cosine foreshortening effect on the angular width of the illuminated spot. The energy resolution of the analyzer was estimated at about 0.2 eV by measuring the sharpness of the Fermi edge in some preliminary calibration experiments on polycrystalline copper.

The ambient magnetic field in the vicinity of the sample and analyzer was cancelled to below 20 mG by means of three orthogonal pairs of coils. Even with these low residual magnetic fields, electrons with kinetic energy less than about 1 eV can still be appreciably deflected. We have therefore attached less significance to the extreme low-energy end of our spectra. It is to be noted that our experimental configuration is immune to the more severe effects of magnetic deflection. The illuminated spot and the various tubes and apertures through which the photoelectrons must pass define, within certain limits, a rectilinear trajectory. Photoelectrons whose trajectories have been curved outside these limits by the residual magnetic field

will not arrive at the detector. In other words, the experimental configuration has a built-in feature which rejects the more excessively deflected electrons. In confirmation of this, we have observed that at the low-energy end, photoelectrons tend to be relatively less abundant in the angular-resolved spectra than in spectra obtained by conventional methods which integrate over the entire solid angle.

The photon energy used in most of our experiments was 10.2 eV. Only a few measurements were made at other photon energies. This was dictated by the time-consuming nature of these experiments. The collection aperture subtends about 0.01% of the total solid angle into which emission occurs and signals are consequently low. We have therefore concentrated our efforts on angular dependences, and deferred detailed investigation of the photon energy dependence for further study. It would also be of interest, in some future study, to investigate the effect of varying the angle of incidence of the light; in the experiments described here, the light was incident normally with an angular spread of several degrees, as indicated in Fig. 5.

The degree of polarization of the light in the present experiments is not known with precision but can be estimated roughly as follows. Measurements by Derbenwick[38] using a monochromator similar to ours indicate that the light emerging from the monochromator is virtually unpolarized. The mean angle of incidence at the ellipsoidal mirror is 75°. From the optical constants of gold at 10.2 eV given by Canfield *et al.*,[39] we deduce that the intensity reflectances for *s*- and *p*-polarized light at this angle of incidence are 65% and 22%, respectively. We conclude therefore that there is a preference in our experiments for the electric vector to be oriented normal to the plane of Fig. 5 to the extent given by these reflectivities. It would be of interest, in future experiments, to investigate systematically the effects of polarization on the angular-resolved photoemission properties.

B. Sample preparation

The samples used in these experiments were single crystals grown at Bell Laboratories by DiSalvo. A thin ribbon, 0.03 mm thick, of copper foil was attached to the edge of the underside of the crystal with a silver-impregnated epoxy cement, Epo-tek 417, in order to establish electrical contact with the sample. Care was taken to avoid curing temperatures at which the 1*T* phase would transform irreversibly to the 3*R* polytype. The underside was then cemented with a nonconducting/quick-drying epoxy cement, Veeco Ve-seal, to the end of a copper rod attached to the end of the main shaft of the precision rotary manipulator. The edges of the crystal were then trimmed with scissors so that the sample had an approximately circular shape with a diameter of about 6 mm. One end of a 0.38-mm-diam copper wire was cemented with Ve-seal to the front face of the crystal, and the other end was fastened to the stationary hemisphere support. The cleave was accomplished by pulling the crystal apart using the longitudinal linear motion of the precision manipulator. The pressure in the vacuum chamber at the time of cleaving was 1×10^{-10} Torr or less. Immediately after cleaving, the sample was advanced to the position shown in Fig. 5 and the photoemission measurements were started. (The cleaving blade indicated schematically in Fig. 5 was not employed in these experiments on layer compounds, but was used in the work on GaAs mentioned earlier and reported elsehwere.[13])

C. Data acquisition

The channel electron multiplier mentioned above was operated at a relatively low gain of about 5×10^5 so that the gain would be count-rate insensitive even for as many as 10^6 electrons incident per second. Pulses emerging from the multiplier were capacitively coupled to a pulse amplifier through a filter network which reduced high-voltage transients and rf pickup. The output of the amplifier was fed into an Ortec 715 Dual Counter/Timer which, in turn, operated under the control of a Nova 1220 minicomputer. The minicomputer was also equipped with digital-to-analog converters which provided the analyzer retarding voltage increments as well as the oscilloscope and *X-Y* plotter displays. Energy distribution curves were obtained in the Nova by subtracting the counts accumulated at successive retarding voltages. A three-point smoothing algorithm was then optionally applied to the data. The spectra presented in this paper have all been three-point smoothed three times. We checked that the spectra attained in this manner were basically the same as those obtained without smoothing from data accumulated for longer periods of time to improve the statistics. The time required to accumulate a typical spectrum was about a half hour.

D. X-ray orientation

After the photoemission measurements on the 1*T* crystals, the orientation of the sample was determined by means of x-ray diffraction. Since the outcome of these x-ray measurements is crucial to much of the discussion in Sec. V, we describe them in some detail. It is to be noted that merely indexing a Laüe photograph without regard to the intensities of the diffraction spots is ambiguous in that it does not distinguish between the orientation shown in Fig. 1 and the inequivalent orientation obtained by a rotation of 180° about the *c* axis. It

was therefore necessary to resort to an intensity analysis of the x-ray diffraction pattern.

In a kinematical treatment of x-ray scattering, the amplitude of the scattered plane wave is given by

$$\psi_{\vec{G}} \propto \sum_i f_i e^{i\vec{G}\cdot\vec{r}_i}, \tag{3}$$

where $\vec{G}$ is the reciprocal-lattice vector separating the incident from the scattered wave vectors; the sum is over the atoms of the unit cell; $\vec{r}_i$ is the position of the ith atom, and f_i is its scattering factor, including anomalous dispersion but neglecting thermal motion.[40]

For the $1T$ unit cell of Fig. 1 with the origin taken at the center of inversion as shown, we have

$$\psi_{\vec{G}} \propto f_{\mathrm{Ta}} + 2f_{\mathrm{Se}} \cos(\vec{G}\cdot\vec{r}_{\mathrm{Se}}). \tag{4}$$

Let the position vector of the outermost (closest to the crystal surface) Se atom in the unit cell be given by

$$\vec{r}_{\mathrm{Se}} = \tfrac{1}{3}\vec{t}_1 + \tfrac{2}{3}\vec{t}_2 + z\vec{t}_3 \equiv (\tfrac{1}{3}, \tfrac{2}{3}, z), \quad 0 < z < \tfrac{1}{2} \tag{5}$$

where the conventional primitive translation vectors are

$$\vec{t}_1 = \frac{a}{2}(\sqrt{3}\,\hat{i} - \hat{j}); \quad \vec{t}_2 = a\hat{j}; \quad \vec{t}_3 = c\hat{k}, \tag{6}$$

and $\hat{i}$, $\hat{j}$, $\hat{k}$ are unit vectors along the x, y and z axes, respectively. The other Se atom in the cell then at $(-\frac{1}{3}, -\frac{2}{3}, -z)$. Let the vectors $\vec{G}$ be given by

$$\vec{G}(hkl) = 2\pi(h\vec{b}_1 + k\vec{b}_2 + l\vec{b}_3) \tag{7}$$

where the $\vec{b}_i$ are the set of vectors reciprocal to the $\vec{t}_i$, and h, k, l are integers. Equation (4) becomes

$$\psi_{\vec{G}(hkl)} = \begin{cases} f_{\mathrm{Ta}} + 2f_{\mathrm{Se}}\cos(2\pi lz) & \text{for } h + 2k \equiv 0 \pmod 3 \\ f_{\mathrm{Ta}} - f_{\mathrm{Se}}[\cos(2\pi lz) \pm \sqrt{3}\,\sin(2\pi lz)] & \text{for } h + 2k \equiv \pm 1 \pmod 3. \end{cases} \tag{8}$$

Equation (8) demonstrates that, for a given l, we may rotate the crystal in the x-ray goniometer about its c axis in increments of 60° and observe six diffraction maxima whose intensities $\psi^*\psi$ alternate between strong and weak values. Table I compares calculated intensities with values determined experimentally for reflections of the type $(01l)$ using Mo $K\alpha$ radiation.

The experimental results for odd l given in Table I alternate from weak to strong in the same sense as the calculated intensities. This establishes that our assignment of $\vec{r}_{\mathrm{Se}} = (\frac{1}{3}, \frac{2}{3}, z)$ is correct, or, to put it another way, our $1T$ crystals are indeed oriented with respect to the x, y, z axes in the manner indicated in Fig. 1.

The results for even l are of some incidental interest. Table I shows that if z were equal to its ideal value of $\frac{1}{4}$, the diffraction spots for even l would display sixfold symmetry. We see, however, that the measured intensities alternate between weak and strong values just as they do for odd l. Also, the sense of the alternation is consistent with a value of z greater than the ideal value of $\frac{1}{4}$, and our best estimate would lie in the range, $z = 0.256 \pm 0.002$. This refined value for z cannot be taken too literally, at this stage, however, since the atomic displacements it implies are comparable with those associated with the superlattice distortions, which have been ignored in our analysis. An important point for our present purposes is that the refinements to z do not influence our determination of the crystal orientation based on

TABLE I. Calculated and measured x-ray reflection intensities in relative units for $1T$-$TaSe_2$. The measured values quoted in the last column are averages of the results at ϕ, $\phi = 120°$, and $\phi + 240°$.

ϕ (deg)	(hkl)	$\psi^*\psi$(calculated) $z = 0.240$	0.250	0.260	$\psi^*\psi$(measured (arbitrary units)
0, 120, 240	(0 1 7)	406	132	59	380
60, 180, 300	(1 0 7)	4416	3918	2902	4800
0, 120, 240	(0 1 9)	1896	2874	3241	3770
60, 180, 300	(1 0 9)	51	108	417	1370
0, 120, 240	(0 1 8)	132	452	1188	2270
60, 180, 300	(1 0 8)	1188	452	132	730
0, 120, 240	(0 1 10)	2648	1746	764	1120
60, 180, 300	(1 0 10)	764	1746	2648	2630

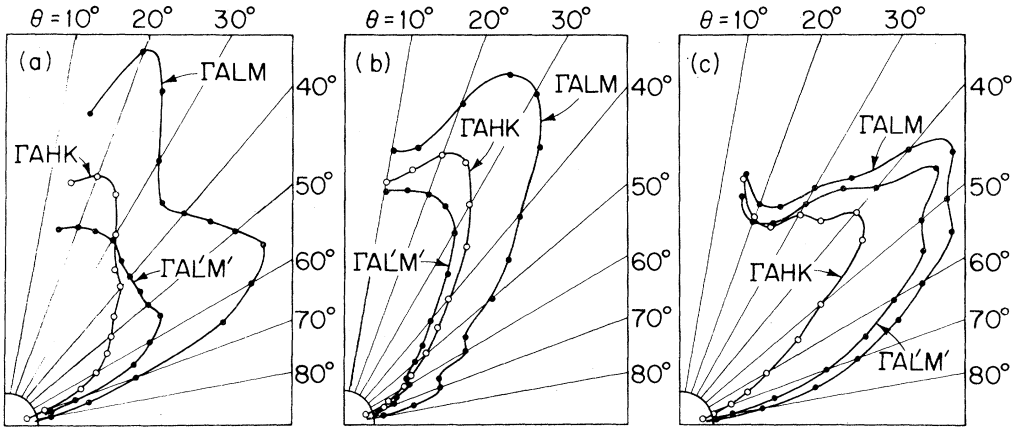

FIG. 6. Polar angle dependence of the photocurrent at $\hbar\omega = 10.2$ eV in the ΓALM, ΓAHK, and $\Gamma AL'M'$ planes for (a) $1T$-$TaSe_2$, (b) $1T$-TaS_2, and (c) $2H$-$TaSe_2$.

the sense of the weak-to-strong alternation of the odd l diffraction maxima.

IV. VARIATIONS WITH POLAR ANGLE

In this section we present results and discussion on the θ dependence of the photoemission properties of the layer compounds studied. Our main emphasis will be on the locations of peaks in the photoelectron energy spectra and their relation to the band structure. Except when otherwise stated, the experimental measurements were performed using a photon energy $\hbar\omega = 10.2$ eV.

A. Photoelectric yield

Experimental results for the θ dependence of the total photocurrent (i.e., electron counting rate at the detector in the absence of any retarding potential) are shown in Figs. 6(a), (b), and (c) for $1T$-$TaSe_2$, $1T$-TaS_2, and $2H$-$TaSe_2$, respectively. In each figure, results are shown for $\phi = 0°$, 30°, and 60°, which correspond, respectively, to moving the analyzer in the ΓALM, ΓAHK, and $\Gamma AL'M'$ planes indicated in Fig. 4. It is seen that the radial plots of the photocurrent display appreciable structure as a function of θ, and that these variations are different in the three different symmetry planes.

In the $1T$ materials, the photocurrent in the ΓALM plane is roughly twice as great as that in the inequivalent $\Gamma AL'M'$ plane. The structure, however, is quite similar. For example, in the $1T$-$TaSe_2$ results of Fig. 6(a), the prominent lobe observed at about $\theta = 55°$ in the ΓALM plane appears also in the $\Gamma AL'M'$ plane but considerably scaled down.

In $2H$-$TaSe_2$, the ΓALM and $\Gamma AL'M'$ planes are no longer inequivalent, and we note in Fig. 6(c) that the measured photocurrents in these two planes are very close to each other. The slight difference between the two curves is quite probably an experimental artifact due to small movements of the illuminated spot over the surface as the sample is rotated. Part of the difference, however, may be due to residual threefold symmetry. In Sec. V F below, we will show that the Ta d-emission displays significant residual threefold symmetry, and that it can be related to the finite sampling depth of the photoemission experiment.

B. Photoelectron energy spectra on $1T$-$TaSe_2$ and $1T$-TaS_2

Experimental results for the θ dependence of the photoelectron energy spectra from $1T$-$TaSe_2$ are shown in Figs. 7(a), 7(b), and 7(c) for the ΓALM, ΓAHK, and $\Gamma AL'M'$ planes respectively. These, and all other spectra in this paper, are referred to initial-state energy, $E - \hbar\omega + \Phi$, where Φ is the work function. This choice of scale places the zero of energy at the Fermi level, E_F. (Strictly speaking, the quantity $E - \hbar\omega + \Phi$ is the initial-state energy only in the absence of effects such as hold relaxation.[41])

Let us consider first the spectra for the ΓALM plane shown in Fig. 7(a). On the basis of previous photoemission work[20-24] and the band structures described in Sec. IB,[17,18,30-37] we identify the small peak seen in some of the spectra between about -1 eV and E_F as emission from the occupied Ta-derived d states. The larger peaks at lower energies are attributed to emission from the Se-derived p states. Qualitatively, we see that the shapes of the spectra vary quite dramatically with θ. A quantitative feature to which we draw particular attention is the movement to lower energies of the uppermost Se p-emission peak as θ is increased. The Ta d-emission peak also shows some tendency to fall to lower energies as θ is increased. In the lower p-emission energy region, a new peak

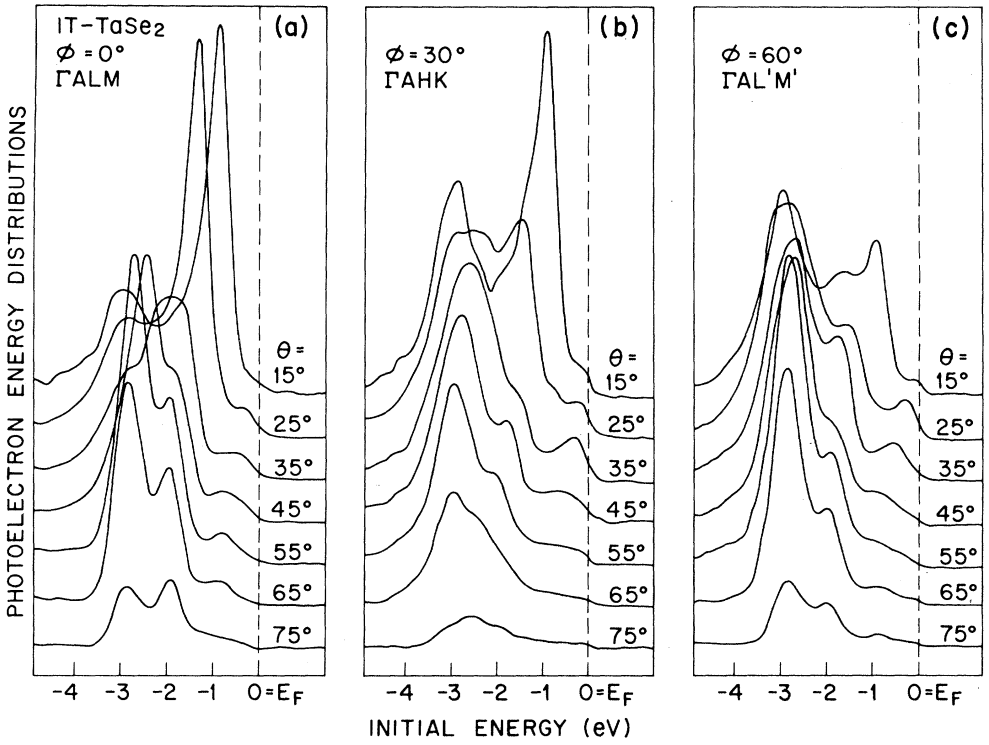

FIG. 7. Photoelectron energy spectra for $1T$-$TaSe_2$ at $\hbar\omega = 10.2$ eV as a function of polar angle θ, for (a) $\phi = 0°$ (ΓALM plane), (b) $\phi = 30°$ (ΓAHK plane), and (c) $\phi = 60°$ ($\Gamma AL'M'$ plane). Spectra are plotted against initial-state energy with the zero taken at the Fermi level.

emerges for θ values above about 35°. This low-energy p-emission peak is responsible for the lobe centered at about 55° in the $\phi = 0°$ yield data of Fig. 6(a).

The θ dependence of the photoelectron energy spectra of $1T$-$TaSe_2$ in the ΓAHK plane is shown in Fig. 7(b). Features are observed very similar to those observed in the ΓALM plane. The uppermost Se p-emission peak, which appears very prominently at about -1 eV in the $\theta = 15°$ spectrum, moves to lower energies as θ is increased.

Photoelectron energy spectra of $1T$-$TaSe_2$ taken in the $\Gamma AL'M'$ plane at various values of θ are shown in Fig. 7(c). These are rather similar to those observed in the ΓALM plane shown in Fig. 7(a), in that structures occur at the same initial energies. The structures in the upper Se p-region, however, are considerably smaller in relative intensity than those observed in the ΓALM plane. This would indicate that the energy levels of the initial states are similar in the ΓALM and $\Gamma AL'M'$ planes, but that the momentum matrix elements for optical transitions may be different.

Experimental results for the θ dependence of the photoelectron energy spectra of $1T$-TaS_2 are shown in Fig. 8 for the ΓALM plane only. The very prominent peak seen at -1.7 eV in the spectrum at $\theta = 15°$ is identified as emission from states near the top of the S-derived p bands. As in $1T$-$TaSe_2$, this uppermost p-emission peak moves to lower energies as θ is increased. The main difference with respect to the $1T$-$TaSe_2$ results is that the S p emission originates from a lower energy relative to the Fermi level than the Se p emission. The prominent features seen in the lower p-emission region of $1T$-$TaSe_2$ are not seen in $1T$-TaS_2. Such effects may occur but, because of the lower relative energy of the S p bands, may be obscured by the threshold cut-off effects. The absence of these low-energy features in $1T$-TaS_2 is consistent with the absence in Fig. 6(b) of the prominent lobe which occurs at $\theta = 55°$ in the photocurrent results of $1T$-$TaSe_2$ in Fig. 6(a).

The small peak which occurs between about -1 eV and E_F is attributed to emission from the Ta d-derived bands. This peak is either absent or only weakly present in the spectrum at $\theta = 15°$, but is quite prominent in the spectrum at $\theta = 25°$. As θ is increased further, this Ta d peak moves to lower initial-state energies. Because of the choice of vertical scale, these effects are not seen to best advantage in Fig. 8. The effects are illustrated more convincingly in Fig. 9, which presents spectra taken in the ΓALM plane at the lower photon

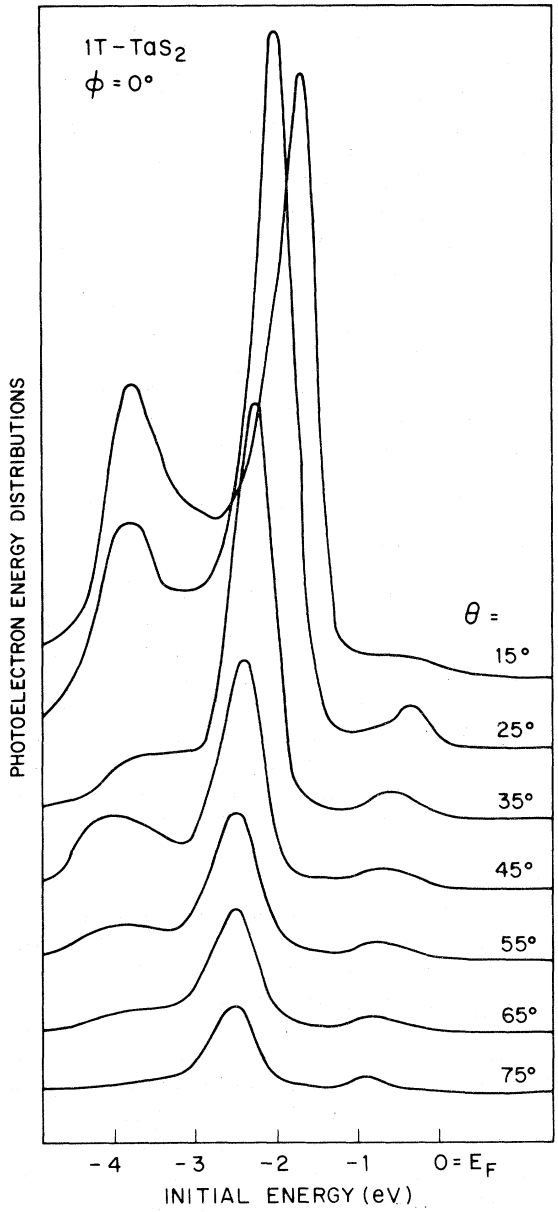

FIG. 8. Photoelectron energy spectra for $1T$-TaS_2 at $\hbar\omega = 10.2$ eV for a sequence of polar angles. The azimuthal angle is kept constant at $\phi = 0°$ (ΓALM plane).

energy of 8.9 eV. At $\theta = 25°$, emission is observed in the energy range -1 eV to E_F, but it is rather featureless, and only the Fermi edge is clearly displayed. At $\theta = 35°$, we observe a well-defined peak at -0.3 eV. As θ is increased, this peak moves to lower energy, and is seen at -0.7 eV in the spectrum at $\theta = 75°$. In this latter spectrum, the peak is observed separate from the Fermi edge. The behavior of this peak is reminiscent of the angular photoemission studies on the (111) face of Ag by Gustafsson *et al.*[4] A peak was observed from the s-p derived levels in Ag which moved with θ in the manner predicted by the band structure. This peak, however, was riding on an angle-insensitive background not predicted by simple theories based on specular refraction. A similar effect appears to be occurring in these experiments.

C. Mapping energy bands

The spectra of Figs. 7(a) and 8 for the ΓALM plane have been used to plot experimental $\mathcal{E}(\vec{k})$ dispersion curves. Our procedure is based on the elementary considerations discussed in Sec. I. For each peak in the spectra taken at $\hbar\omega = 10.2$ eV, we determined the kinetic energy E at the maximum of that peak. The parallel wave vector $\vec{k}_{\parallel}$ corresponding to each of these values for E, was evaluated from the simple formula

$$k_{\parallel} \equiv (k_x^2 + k_y^2)^{1/2} = (2Em/\hbar^2)^{1/2} \sin\theta. \tag{9}$$

We then plotted the initial-state energy $E - \hbar\omega + \Phi$ versus $k_{\parallel}$, and the results are represented by the filled and open circles in Figs. 10(a) and 10(b).

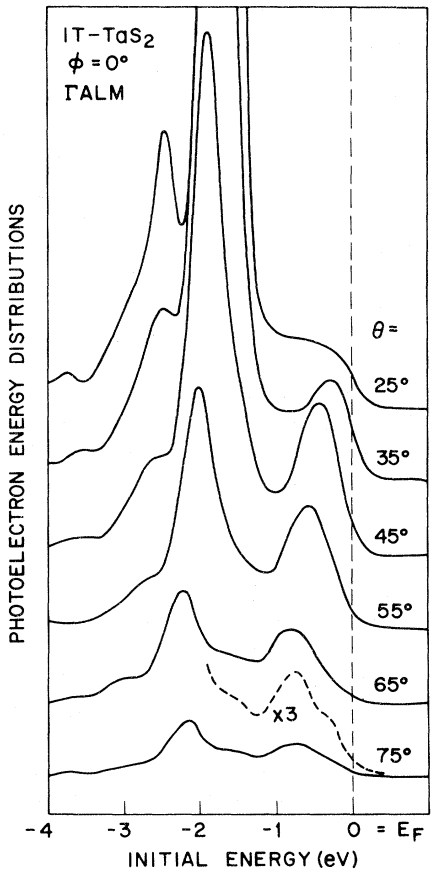

FIG. 9. Photoelectron energy spectra for $1T$-TaS_2 at $\hbar\omega = 8.9$ eV for a sequence of polar angles. The azimuthal angle is kept constant at $\phi = 0°$ (ΓALM plane).

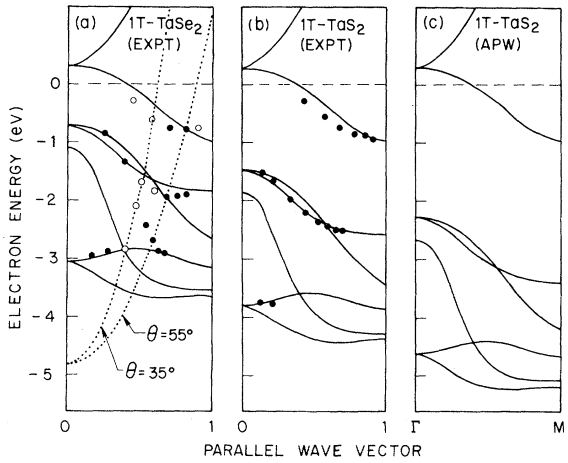

FIG. 10. Electron energy vs parallel wave vector: (a) experimental results for $1T$-$TaSe_2$ (full and open circles); (b) experimental results for $1T$-TaS_2 (full circles); (c) APW results of Mattheiss (Ref. 18) on $1T$-TaS_2. In (a) and (b), wave vectors are expressed in units of the Γ to M distance. The smooth curves included in (a) and (b) are those of (c) except that the chalcogen p bands have been given a rigid shift to higher energies.

Filled circles represent peaks with well-defined maxima; open circles represent weaker peaks or shoulders.

The basic assumptions in this procedure are as follows. It is assumed that the refraction at the boundary is specular, so that $\vec{k}_{\parallel}$ is the same both inside and outside the material. It is assumed also that the optical transitions are direct, so that the initial state at energy $E-\hbar\omega+\Phi$ may be assigned the same value for $\vec{k}_{\parallel}$ as that determined for the final state. We concentrate here on the initial-state energy rather than the final-state energy since the assumption of flatness of the bands in the k_z direction is likely to have greater validity for the occupied bands than the final-state bands. In other words, leaving k_z indeterminate is of less consequence as far as the initial-state bands are concerned.

We note that, for an individual spectrum in Figs. 7 or 8, θ remains constant. It follows that, in a plot of $E-\hbar\omega+\Phi$ versus $(2mE/\hbar^2)^{1/2}\sin\theta$, points obtained from the same spectrum must lie on a parabola. Two such parabolae (for $\theta=35°$ and $55°$) are shown as dotted curves in Fig. 10(a). In the spectra used here, $k_{\parallel}$ is always within the first Brillouin zone. The need to translate wave vectors back into the reduced zone, as discussed earlier[13,19] does not arise in this work.

The APW energy bands calculated by Mattheiss for the ΓM direction in $1T$-TaS_2 are shown in Fig. 10(c). This is merely a portion of the more detailed results illustrated in Fig. 2. These bands display trends in good agreement with the experimentally derived bands shown in Fig. 10(b). In particular, the energies in the uppermost p band and the occupied d band decrease with increasing $k_{\parallel}$ in both theory and experiment. The main point of difference concerns the position of the S-derived p bands relative to the Ta-derived d bands. As shown in Fig. 10(b), better agreement is obtained for $1T$-TaS_2 if Mattheiss' p bands are given a rigid shift of 0.8 eV to higher energies. This is consistent with the result obtained in the x-ray photoemission spectroscopy measurements of Wertheim *et al.*[23]

Likewise, in $1T$-$TaSe_2$, if we assume that Mattheiss' results for $1T$-TaS_2 represent a good first approximation to the band structure, it is seen in Fig. 10(a) that a rigid shift of the chalcogen p bands by 1.6 eV to higher energies is required to secure alignment between theory and experiment for the position of the upper p bands. Once this adjustment has been made, the peaks observed in $1T$-$TaSe_2$ at about -2.9 eV also fall very close to one of the lower p bands in Mattheiss' calculation. Between the uppermost p peaks and these peaks at about -2.9 eV, there is a third piece of experimental structure in the -2.1 to -2.7-eV range, which decreases in energy quite rapidly with increasing $k_{\parallel}$. This may correspond to the calculated band in Fig. 10(a) whose energy is -1.1 eV at $k_{\parallel}=0$ and which also falls rapidly as $k_{\parallel}$ increases. The calculated band occurs, however, at a consistently lower $k_{\parallel}$ than the experimental band. This discrepancy is not disturbing since, in Mattheiss' calculations, this particular band is markedly nonflat in the k_z direction, and so our assumptions are less likely to apply. On the other hand, this intermediate piece of structure may correspond to the calculated band which occurs at consistently higher $k_{\parallel}$. The discrepancy in the values of $k_{\parallel}$ might then be attributed to the approximations involved in the use of a simple rigid shift of the p bands.

We have chosen to compare our experimental results with the energy bands along the ΓM direction, but it would have been equally valid to have considered the AL direction (or any direction with the same set of values for $k_{\parallel}$). Results have been presented here only for the ΓALM plane. In the ΓAHK plane, the agreement with Mattheiss' calculations is less satisfactory owing to the appearance of some unexpected d emission. This is discussed below in Sec. V E.

D. Photoelectron energy spectra on $2H$-$TaSe_2$

Experimental results for the θ dependence of the photoelectron spectra of $2H$-$TaSe_2$ are shown in Figs. 11(a) and 11(b), which correspond, respectively, to moving the analyzer in the ΓALM ($\phi=0°$) and ΓAHK ($\phi=30°$) planes. Spectra taken in the

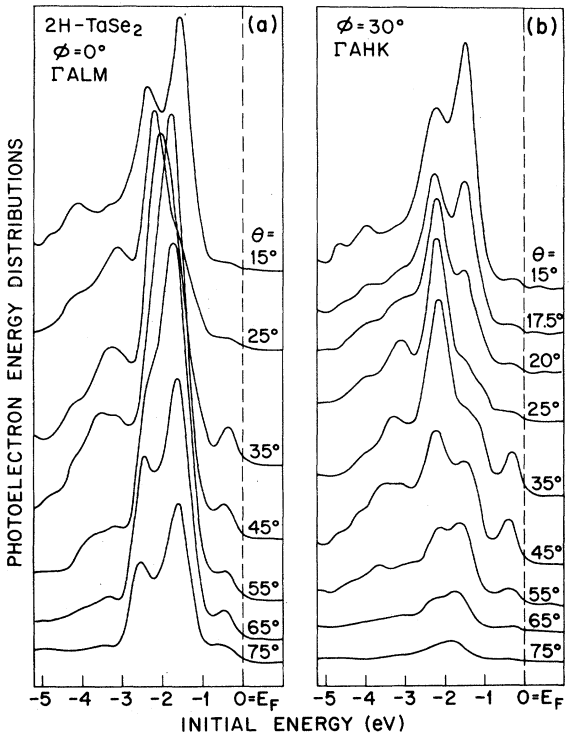

FIG. 11. Photoelectron energy spectra for $2H$-$TaSe_2$ at $\hbar\omega = 10.2$ eV as a function of polar angle for (a) $\phi = 0°$ (ΓALM plane) and (b) $\phi = 30°$ (ΓAHK plane).

$\Gamma AL'M'$ ($\phi = 60°$) plane were found to be similar to those in the ΓALM plane and are therefore not shown. (As mentioned in Sec. IB, the $\Gamma AL'M'$ plane is entirely equivalent to the ΓALM plane in the $2H$ polytype; we retain the primed labels merely for convenience.) The small peak which appears in some of the spectra between -1 eV and E_F is once again identified as emission from the Ta-derived d states. Note that for $\theta \leq 25°$, the emission in this region is weak and featureless, but at $\theta = 35°$ there is a prominent peak. This abrupt appearance of the Ta d-peak is reminiscent of the behavior for $1T$-TaS_2 illustrated in Fig. 9.

The behavior in the p-emission region of $2H$-$TaSe_2$ differs quite appreciably from that in $1T$-$TaSe_2$. At $\theta = 15°$ in the ΓALM plane [Fig. 11(a)], we observe two strong peaks in the p-emission region of $2H$-$TaSe_2$. The upper peak at -1.55 eV is the stronger at $\theta = 15°$, but becomes weaker as θ is increased. The lower peak occurs at -2.35 eV at $\theta = 15°$, and moves to higher energies as θ is increased. At $\theta = 35°$, the two peaks appear to have coalesced into a single peak located at -2.0 eV. As θ is increased further, two peaks are resolved again, and the lower one moves to lower energies with increasing θ.

In the ΓAHK plane for $2H$-$TaSe_2$ [Fig. 11(b)], the spectrum at $\theta = 15°$ is similar to that in the ΓALM plane in that two strong peaks are observed at -1.5 and -2.25 eV. The behavior on increasing θ is less dramatic than in the ΓALM plane. The upper peak decreases in relative intensity as θ is increased, whereas the lower peak increases in intensity. While there is some slight movement in energy location, the coalescence observed in the ΓALM plane does not occur in the ΓAHK plane.

A feature which the spectra in the ΓALM and ΓAHK planes of $2H$-$TaSe_2$ share in common, and which is significantly different from the behavior in $1T$-$TaSe_2$, concerns the upper edge of the Se p-emission contribution. In $2H$-$TaSe_2$, the energy location of this edge remains fairly stationary as θ is varied. In $1T$-$TaSe_2$ (Fig. 7), on the other hand, the upper edge of the p-emission moves to lower energies with increasing θ. We will see that this qualitative difference is consistent with the predictions of the band calculations.

Experimental $\mathcal{E}(\vec{k})$ dispersion relations were plotted for $2H$-$TaSe_2$ in the ΓALM plane using the same mapping procedure described above. The results are shown as the filled and open circles in Fig. 12. The smooth curves in Fig. 12 represent the ΓM portion of the calculated energy bands of Mattheiss for $2H$-TaS_2 (Fig. 3). The chalcogen p bands, however, have been given a rigid shift of

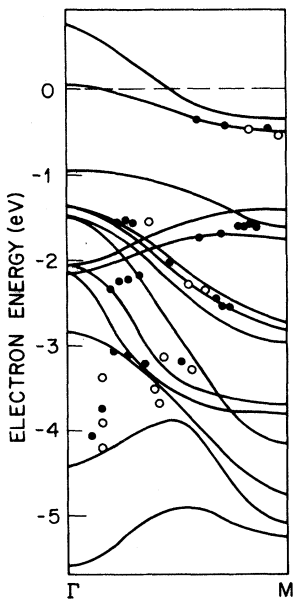

FIG. 12. Energy bands for $2H$-$TaSe_2$. The full and open circles represent the experimental results obtained in the ΓALM plane [Fig. 11(a)]. The smooth curves represent the APW results of Mattheiss (Ref. 18) for $2H$-TaS_2; the chalcogen p bands have been shifted upwards rigidly by 0.9 eV.

0.9 eV to higher energies relative to E_F. We are assuming here, as before, that the energy bands of the disulfide represent a good first approximation to the energy bands of the diselenide. After this adjustment has been performed, we observe some encouraging correspondence between theory and experiment. The calculated band structure shows three closely spaced bands which occur in the range -1.4 to -1.5 eV at Γ, fall in energy as $k_{\parallel}$ is increased, and occur in the range -2.7 to -3.0 eV at M. We associate these bands with the downward-trending set of experimental points representing the downward-moving peak in Fig. 11(a). The rigid shift of 0.9 eV was chosen partly to achieve this alignment in Fig. 12. The calculated band structure shows two closely spaced bands which start in the range -2.2 to -2.0 eV at Γ and move upwards in energy into the range -1.8 to -1.4 eV at M. We associate this pair of bands with the upward-moving set of experimental points corresponding to the other prominent p-emission peak in Fig. 11(a). The agreement in position is quite good, particularly near the M point. In this interpretation, the coalescence of the two prominent p-emission peaks at about $\theta = 35°$ is due to the crossing of the two upward-moving bands with the three downward-moving bands. The existence in the calculations on $2H$-TaS_2 of these bands which move upwards with increasing $k_{\parallel}$ serves to explain the roughly constant energy of the upper edge of the p emission in the experimental spectra. In TaS_2, on the other hand, the calculated energy of the upper p bands invariably decreases with increasing $k_{\parallel}$, consistent with the strong movement of the upper edge of the p emission in $1T$-TaS_2 and $1T$-$TaSe_2$.

The experimental bands for $2H$-$TaSe_2$ just below -3.0 eV also show some correspondence with the adjusted theoretical bands. Finally, the experimental d-emission peak falls close to the lower of the two theoretical d bands. The abrupt appearance of the d peak at about $\theta = 35°$, however, is more consistent with the behavior of the upper theoretical band since it falls below E_F only for values of $k_{\parallel}$ greater than about 45% of the Γ to M distance.

V. VARIATIONS WITH AZIMUTHAL ANGLE

In this section, we consider the azimuthal dependence of photoemission. Our emphasis will be on intensities rather than peak positions. In attempting to interpret the experimental results it is necessary to go beyond the $\mathcal{E}(\vec{k})$ relations and consider also the wave functions of the initial and final states of the optical transitions which give rise to the photoelectrons.

A. Photoelectric yield

The azimuthal dependence of the photoelectron counting rate for electrons of all energies is shown for three values of θ in Figs. 13(a), (b), and (c) for $1T$-$TaSe_2$, $1T$-TaS_2, and $2H$-$TaSe_2$, respectively. These figures are the azimuthal counterparts of the polar dependence results of Fig. 6. At $\theta = 55°$, the azimuthal dependence of the photocurrent in $1T$-$TaSe_2$ displays three major lobes centered about the ΓALM planes and minor lobes about the $\Gamma AL'M'$ planes. At $\theta = 25°$ and $35°$, the azimuthal anisotropy in $1T$-$TaSe_2$ is weaker than at $\theta = 55°$ but still displays strong threefold rotational symmetry.

The results for $1T$-TaS_2 are similar to those for $1T$-$TaSe_2$, with the difference that the relative intensity of emission at $\theta = 55°$ is smaller. This is consistent with the considerations in Sec. IV A and IV B, where it was pointed out that the strong lobe

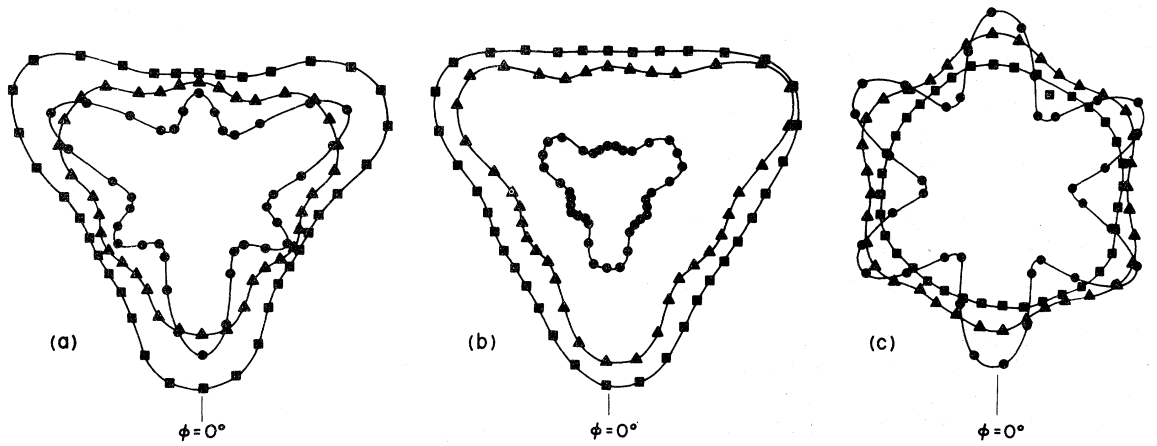

FIG. 13. Azimuthal dependence of the photocurrent at $\theta = 25°$ (filled squares), $\theta = 35°$ (filled triangles), and $\theta = 55°$ (filled circles) for (a) $1T$-$TaSe_2$, (b) $1T$-TaS_2, and (c) $2H$-$TaSe_2$. Smooth curves have been drawn to connect the points.

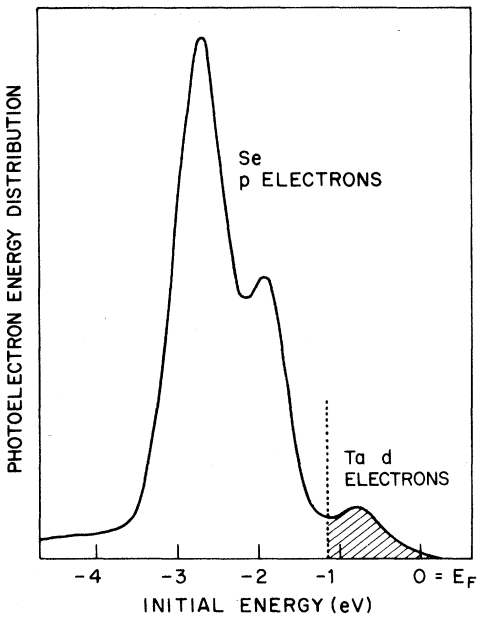

FIG. 14. Energy spectrum of photoelectrons emitted from $1T$-$TaSe_2$ at $\hbar\omega = 10.2$ eV at the angles $\theta = 55°$ and $\phi = 0°$. The cross-hatched area is taken as a measure of the Ta d-emission intensity.

in the θ dependence of the photocurrent in $1T$-$TaSe_2$ is associated with emission from lower-lying p states, and that in $1T$-TaS_2 this emission is attenuated by threshold cut-off effects. It appears that emission from these lower-lying p states is responsible also for strong azimuthal anisotropies in the photocurrent.

In $2H$-$TaSe_2$ [Fig. 13(c)], the results at $\theta = 55°$ display the strongest azimuthal anisotropy, and the relative intensities of the $\theta = 55°$ lobes are close to those at $\theta = 55°$ in $1T$-$TaSe_2$. The rotational symmetry, however, is sixfold, consistent with the hexagonal crystal structure of this polytype.

B. Ta d-emission intensity in $1T$-$TaSe_2$ and $1T$-TaS_2

A series of experiments was undertaken in which we isolated the Ta d-emission contribution to the photoelectron energy spectrum and examined its azimuthal dependence . In Fig. 14 we show a photoelectron energy spectrum obtained on $1T$-$TaSe_2$ at $\theta = 55°$ in the ΓALM plane. The Ta d emission gives rise to a well-defined peak. The cross-hatched area in the energy "window" from -1.15 eV to 0.0 eV will be taken as our estimate of the Ta d-emission intensity. This area is very readily measured in our particular experimental arrangement by setting the retarding potential at a value corresponding to the dotted vertical line in Fig. 14. The Se p emission is thereby rejected, and the remaining electron-counting rate is a direct measure of the Ta d-emission intensity. Measurements of the actual energy spectra revealed that the energy location of the Ta d peak remains above -1 eV for all values of ϕ. Variations in the cross-hatched area as a function of ϕ are therefore representative of variations in the actual d-emission intensity and are not due to the d peak moving in and out of the energy window.

The outer curve in Fig. 15 is a radial plot of the azimuthal dependence of the total photoelectron counting rate at $\theta = 55°$; this curve corresponds to the total area under the photoelectron energy spectrum and, as already mentioned, it displays quite conspicuously the threefold rotational symmetry of the crystal. Since the Ta d-emission is only a small fraction of the total in $1T$-$TaSe_2$, the outer curve in Fig. 15 may be thought of as the Se p-emission. The inner curve of Fig. 15 represents, on a five-times expanded scale, the azimuthal dependence of the Ta d-emission. Three pairs of major lobes are seen centered about the $\phi = 0°$, 120°, and 240° positions (ΓALM planes), and indications of three pairs of minor lobes are seen centered about the $\phi = 60°$, 180°, and 300° positions ($\Gamma AL'M'$ planes).

The x-ray diffraction studies of Sec. III D revealed that the photoemission pattern is oriented with respect to the crystal structure in the manner shown in Fig. 16. This figure shows the two outermost atomic sheets of $1T$-$TaSe_2$, and the radial plot of the Ta d-emission intensity has been centered on a Ta atom. If one adopts a localized picture and assumes that these photoelectrons are actually cre-

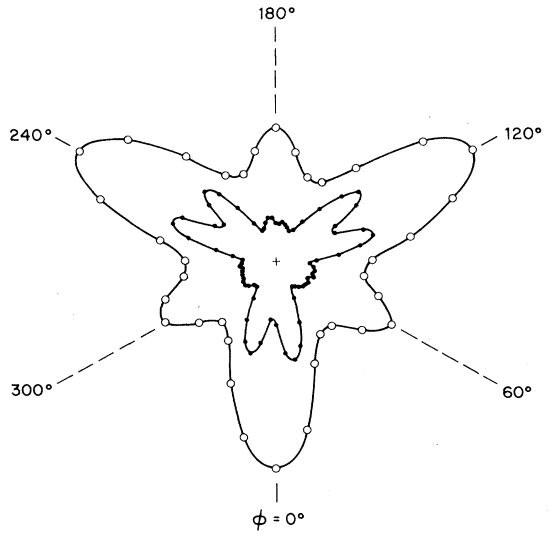

FIG. 15. Radial plots of the azimuthal dependence at $\theta = 55°$ of the total photoemission intensity (open circles) and, on a 5X expanded scale, the Ta d-emission intensity (full circles) taken on $1T$-$TaSe_2$ at $\hbar\omega = 10.2$ eV.

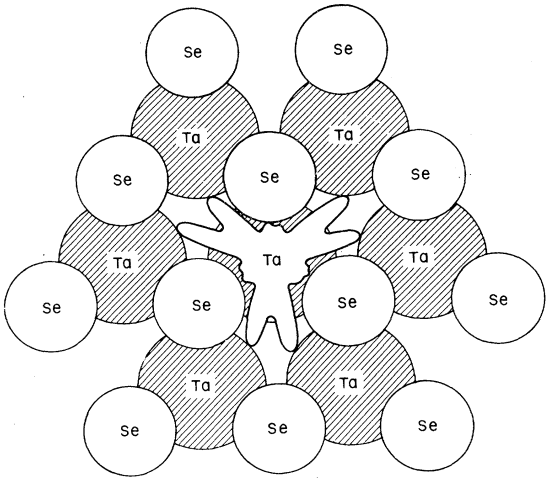

FIG. 16. The experimental Ta d-emission plot for $1T$-$TaSe_2$ at $\hbar\omega = 10.2$ eV at $\theta = 55°$ superposed on the two outermost atomic sheets of the crystal structure.

ated on Ta sites, it is seen from Fig. 16 that they propagate preferentially in directions between the nearest-neighbor Se atoms rather than along the Ta-Se bonds. We note also that the bifurcation into pairs of major lobes corresponds to those trajectories which avoid both first- and second-nearest-neighbor Se atoms.

C. Shadowing effects in the final state

The azimuthal anisotropies observed in the Ta d-emission results of Fig. 16 suggest that Se atoms are opaque to photoelectrons of this particular energy and cast shadows. This shadowing hypothesis receives support from further experiments on $1T$-TaS_2 in which the lobe structure of the d-emission was investigated as a function of θ. $1T$-TaS_2 is a more suitable candidate for a study of this kind than $1T$-$TaSe_2$ owing to the larger energy separation of the Ta d-emission and chalcogen p-emission. In $1T$-$TaSe_2$, it is difficult to separate the d-emission at low values of θ since it tends to be overlapped by the Se p-emission. This problem is alleviated in $1T$-TaS_2, where the edge of the chalcogen p-emission occurs at lower energies, and it is possible to separate the Ta d-emission even at low values of θ.

The results for the θ dependence of the lobe structure of the Ta d-emission are illustrated in Fig. 17. At $\theta = 15°$ (not shown), the radial plot is quite close to a circle; this corresponds to Ta d-photoelectrons emerging almost normal to the surface and without obstruction from the S neighbors. At $\theta = 25°$, indicated by open squares in Fig. 17, a rather broad bulge appears in the $\phi = 0°$ direction, and corresponds to the shadowing effect of the nearest S neighbors. At $\theta = 35°$, indicated by open triangles in Fig. 17, the bulge splits into two lobes separated by 36°. The bifurcated lobe structure becomes more pronounced as θ is increased further. On the shadowing hypothesis, we interpret the valley between the lobes as the shadow cast by the second-nearest S neighbors.

It is of interest to speculate on what would happen if the photon energy could be varied continuously over a wide range. We would expect that for some final-state energies the Se atoms would be transparent as in the Ramsauer-Townsend effect. Such experiments could be accomplished by the use of synchrotron radiation. We anticipate some valuable connections with theoretical and experimental work on the phenomenon of extended x-ray absorption fine structure (EXAFS). Sayers *et al.*[42] have shown how EXAFS is related to multiple scattering effects in the wave function of a photoelectron as it radiates outwards from its atom of origin—a situation very similar to that envisaged here. Indeed, Liebsch[43] has already formulated a theory of angu-

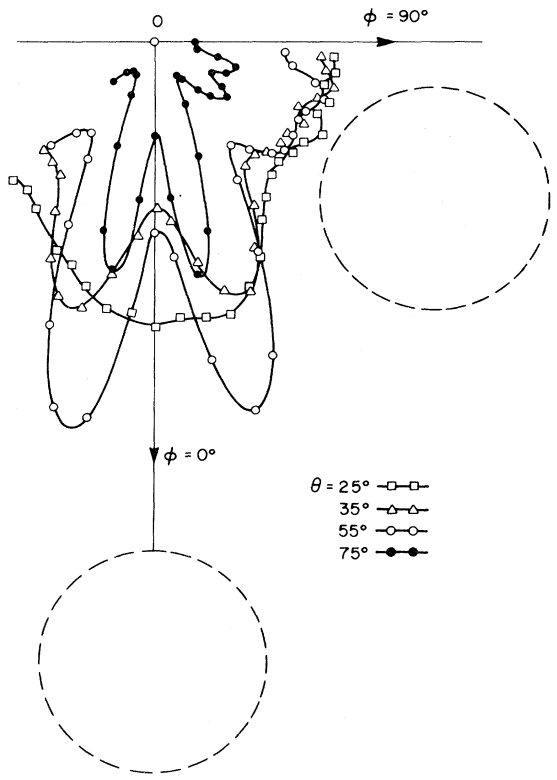

FIG. 17. Azimuthal dependence of the Ta d-emission intensity from $1T$-TaS_2 at $\hbar\omega = 10.2$ eV for various polar angles. The origin 0 represents the center of a Ta atom as in Fig. 16; dashed circles indicate first- and second-nearest-neighbor S atoms.

lar-resolved photoemission which incorporates these effects.

D. Initial states and atomic orbitals

In Sec. V C we have emphasized the role of the final states in producing the observed anisotropies. In this section, we will discuss the results from a point of view which emphasizes the properties of the initial states in the optical transitions. We follow very closely the approach of Gadzuk.[44]

Let us represent an observed photoelectron by the plane wave $e^{i\vec{r}\cdot\vec{r}}$. Neglecting refraction at the boundary and band-structure effects, let us also assume that $e^{i\vec{r}\cdot\vec{r}}$ will serve also as the final state, $|f\rangle$, in the optical transition which gave rise to the photoelectron. This key assumption deliberately deemphasizes the final-state effects, and tends to isolate the role of the initial state in producing the observed anisotropies. Let us represent the initial state in a typical optical transition by a tight-binding Bloch sum over lattice sites $\vec{R}_l$,

$$|i\rangle = \sum_l \phi(\vec{r}-\vec{R}_l)e^{i\vec{k}\cdot\vec{R}_l} . \tag{10}$$

The wave function $\phi(\vec{r})$ represents the appropriate atomic Ta d orbital or combination of atomic orbitals. The contribution $I_k(\vec{p})$ of this transition to the observed intensity of photoelectrons with wave vector $\vec{p}$ will be proportional to $|\langle f|\vec{\nabla}\cdot\vec{A}|i\rangle|^2$, where $\vec{A}$ is the vector potential of the incident radiation. It is then easy to show that

$$I_k(\vec{p}) \propto A^2p^2\langle\cos^2\gamma\rangle\,|\phi(\vec{p})|^2\delta(\mathcal{E}_f-\mathcal{E}_i-\hbar\omega)\sum_{\vec{G}}\delta(\vec{k}-\vec{G}-\vec{p}), \tag{11}$$

where

$$\phi(\vec{p}) = \int e^{i\vec{r}\cdot\vec{r}}\phi(\vec{r})\,d^3r \tag{12}$$

and is simply the momentum representation of the orbital $\phi(\vec{r})$. The sum is over all reciprocal-lattice vectors $\vec{G}$. The $\cos\gamma$ term involves the angle γ between the vectors $\vec{p}$ and $\vec{A}$. Since the radiation is not polarized, we must take the average $\langle\cos^2\gamma\rangle$ which happens to be a constant for our apparatus provided θ is held constant. This is a consequence of our particular experimental configuration. Since we choose to rotate the sample rather than the analyzer in order to vary ϕ, it follows that $\langle\cos^2\gamma\rangle A^2p^2$ does not vary and may therefore be factored out. The main result expressed in Eq. (11) is that *the angular dependence of the photoemission intensity will have impressed upon it the angular dependence of the orbital* $|\phi(\vec{p})|^2$. Speaking more generally, the angular distribution of photoemission intensity is, in this simple picture, a map of the momentum density of the initial-state wave function. The crucial assumption here, of course, is the use of a plane wave $e^{i\vec{r}\cdot\vec{r}}$ for the final-state wave function.

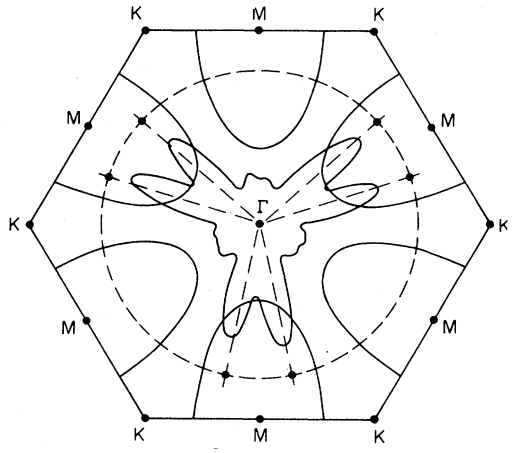

FIG. 18. The experimental Ta d-emission plot superposed on the $k_z=0$ plane of the Brillouin zone. The points of intersection between the broken circle and the broken radial lines represent the estimated mean k-space locations of the optical transitions contributing to the major lobes.

The second δ function in Eq. (11) embodies the requirement of $\vec{k}$ conservation in the optical transition. This is purely a band-structure effect and would apply even if we had used a more elaborate form for the final-state wave function. The requirement of $\vec{k}$ conservation is considered further in Fig. 18, where we have superposed the radial pattern of the Ta d-emission of 1T-$TaSe_2$ at $\theta=55°$ onto the $k_z=0$ plane of the Brillouin zone. The average kinetic energy of these photoelectrons leads to an estimate of the parallel component of $\vec{p}$, and the broken circle in Fig. 18 has been constructed with a radius of this magnitude. Broken radial lines have been drawn along the centers of the major lobes. The points of intersection between the circle and radial lines therefore represent the mean k-space locations (at least in two dimensions) of the optical transitions which gave rise to the observed photoelectrons. Reassuringly, these points fall inside the Fermi surface which, as indicated in Fig. 18, consists of electron pockets centered about the M points[45]; i.e., the occupied Ta d states reside within these pockets.

An important feature of the Ta d emission is the conspicuous threefold rotational symmetry. As mentioned in Sec. II B, the assumption of flatness, of the bands in the k_z direction leads one to expect a sixfold symmetry for the energy bands, at least for the occupied levels. Pairs of lobes centered about the $\phi=60°$, 180°, and 300° are detected, but they are considerably less intense than the major lobes. In terms of the initial-state picture outlined above, we attribute the strong threefold symmetry to the modulating effect of the $|\phi(\vec{p})|^2$

terms of Eq. (11). Referring back to Fig. 16, this would imply that the momentum density of the occupied Ta d orbitals is piled up in directions between the nearest-neighbor Se atoms rather than along the Ta-Se bonds. We explore now the extent to which this is consistent with our present knowledge of the nature of the occupied Ta d orbitals. We note that the angular dependence of an atomic orbital is the same in both real space and momentum space.[46]

In the absence of more detailed calculations, we adopt here a crystal-field or ligand-field philosophy. We assume perfect octahedral coordination and employ the primed coordinate system of Fig. 1 in which the x', y', z' axes are taken along Ta-Se bond directions. In this coordinate system, crystal-field splitting will result in a lower energy for the three degenerate t_{2g} orbitals (i.e., those orbitals whose angular dependences are $x'y'/r^2$, $y'z'/r^2$, and $z'x'/r^2$) than for the two degenerate e_g orbitals [whose angular dependences are $(3z'^2 - r^2)/r^2$ and $(x'^2 - y'^2)/r^2$]. Since there is only one Ta d electron available, this simple crystal-field picture implies partial but equal occupancy of each of the t_{2g} orbitals. This is reasonably consistent with the orbital decomposition of the densities of states calculated by Mattheiss.[18] Mattheiss shows that the centers of gravity of the subbands based on the "t_{2g}" orbitals $x^2 - y^2$, xy, and $3z^2 - r^2$ are close to each other and are considerably lower in energy than the center of gravity of the subband based on the "e_g" orbitals yz and zx. In the true band situation, however, these basis states are mixed with each other in proportions which depend on position in k space. To represent the occupied levels as the t_{2g} states of the crystal-field approach is therefore only a rough approximation, but it is of some interest to see how far it goes in explaining some of the observed anisotropies.

We note here that, in the x, y, z coordinate system, the orbitals $3z^2 - r^2$, $x^2 - y^2$, and xy, sometimes referred to as the t_{2g} orbitals, are only loosely describable as such. The true t_{2g} content is given by the following equations:

$$d_{3z^2-r^2} = (d_{x'y'} + d_{y'z'} + d_{z'x'})/\sqrt{3}\ ,$$
$$d_{x^2-y^2} = (2d_{x'y'} - d_{y'z'} - d_{z'x'} + \sqrt{3}d_{3z'^2-r^2})/3,$$
$$d_{xy} = -(d_{y'z'} + d_{z'x'} + d_{x'^2-y'^2})/\sqrt{3}\ . \qquad (13)$$

It is seen that the orbitals $d_{x^2-y^2}$, d_{xy} are not entirely of t_{2g} character but have a one-third intensity admixture of the e_g orbitals $d_{3z'^2-r^2}$ and $d_{x'^2-y'^2}$, respectively. Likewise, in performing the inverse transformation of coordinates, it is found that the true t_{2g} orbitals, $d_{x'y'}$, $d_{y'z'}$, and $d_{z'x'}$ are composed primarily of the $d_{3z^2-r^2}$, $d_{x^2-y^2}$, and d_{xy} orbitals but have a slight admixture of d_{yx} and d_{zx}. Mattheiss has emphasized the importance of including properly the d-d hybridization effects within the "t_{2g}" subband since they are responsible, in some cases, for the gross qualitative features of the bands.[18] Further to this, our simple analysis above indicates that d-d hybridization between the "t_{2g}" and "e_g" orbitals is also likely to be of importance, since some admixture of the "e_g" orbitals is required in the occupied states if only to satisfy symmetry in the octahedral crystal-field limit.

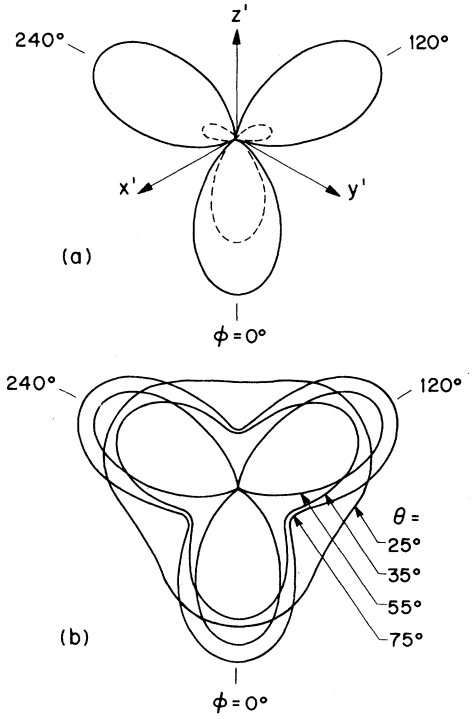

FIG. 19. (a) Azimuthal dependence at $\theta = 55°$ of the intensity of the t_{2g} orbitals; the dashed curve represents the orbital whose angular dependence goes as $x'y'/r^2$; the full curve represents the total intensity of all three t_{2g} orbitals. (b) Azimuthal dependence of the total t_{2g} intensity at various values of θ.

The ϕ dependence at $\theta = 55°$ of the t_{2g} orbital $|d_{x'y'}|^2$ is shown as the dashed curve Fig. 19(a). The full curve in Fig. 19(a) represents the angular dependence of the sum of the intensities of the three t_{2g} orbitals at $\theta = 55°$. The total intensity of the t_{2g} orbitals at several other values of θ is shown in Fig. 19(b). In each curve, three broad lobes are observed centered about the $\phi = 0°$, 120°, and 240° directions, consistent with the stronger weight of the major lobes in the measured d emission. The angular dependence of the t_{2g} orbitals, however, does not display the bifurcation into pairs of lobes as observed experimentally.[47] We must therefore look beyond crystal-field effects for an explanation of the bifurcation.

One possible explanation for the bifurcation is

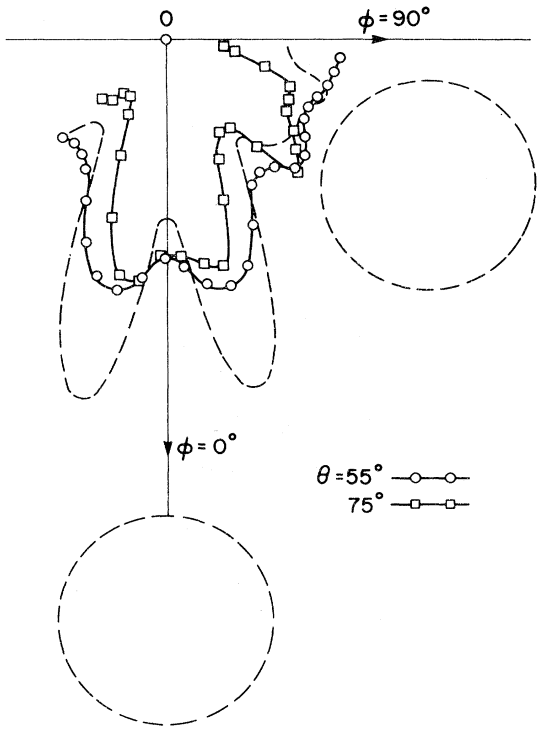

FIG. 20. Azimuthal dependence of the Ta d-emission intensity from $1T$-TaS_2 at $\hbar\omega = 7.8$ eV for $\theta = 55°$ (open circles) and $\theta = 75°$ (open squares); smooth curves have been drawn to connect the points; the dashed curve represents, for comparison, the results for $\theta = 55°$ at $\hbar\omega = 10.2$ eV. As in Fig. 17, the dashed circles represent the positions of first- and second-nearest-neighbor S atoms with respect to a Ta atom at the origin 0.

that it is a band structure effect and arises through the $\vec{k}$-conservation requirement that the optical transitions be confined to certain regions of $\vec{k}$ space as indicated in Fig. 18. Some support for this conjecture is to be found in the photon energy dependence of the lobe structure. The ϕ dependence of the Ta d emission at $\hbar\omega = 7.8$ eV is shown in Fig. 20 for $\theta = 55°$ and $= 75°$. As in the results at $\hbar\omega = 10.2$ eV, pairs of major lobes are observed centered about $\phi = 0°$, and indications of pairs of minor lobes are seen centered about $\phi = 60°$. Also the total angular extent of the pair of major lobes is smaller at $\theta = 75°$ than it is at $\theta = 55°$. The lobes, however, are less well developed at $\hbar\omega = 7.8$ eV than in the corresponding curves at 10.2 eV. Qualitatively, differences of this kind are to be expected from considerations of the $\vec{k}$-conservation requirements in the optical transition and in the photoelectric escape process. First of all, since the kinetic energies of the Ta d photoelectrons are smaller at $\hbar\omega = 7.8$ eV, $k_{\parallel}$ will also be smaller than in curves for the same θ at $\hbar\omega = 10.2$ eV. Secondly, the perpendicular components k_z may also be different, due to the movement through $\vec{k}$ space of the surface of constant interband energy difference as $\hbar\omega$ is varied.

E. Forbidden d emission

We draw attention here to certain features of the experimental results which do not permit of simple interpretations such as those given above. We refer to the failure of the Ta d emission in $1T$-$TaSe_2$ and $1T$-TaS_2 to disappear at certain angles where the calculated band structure predicts that it should. It is apparent from Fig. 10 that below a certain value of θ the Ta d emission in the ΓALM plane should disappear, because the d band is unoccupied for small values of $k_{\parallel}$. The experimental spectra of Figs. 7(a), 8, and 9 do indicate an abrupt drop in the d-peak intensity. The d emission does not disappear entirely, however, but is still present at θ in the form of a featureless background.

A more serious problem arises with the azimuthal dependence of the d emission. The band structure for $1T$-TaS_2 in Fig. 2 predicts that there should be no occupied Ta d states along the ΓK or AH direction. We note in Fig. 18 that the measured Ta d-emission for $1T$-$TaSe_2$ shows well-defined minima in the six ΓK directions but does not drop to zero. (The results for $1T$-TaS_2, part of which are shown in Fig. 17, are the same in this respect.) It may be seen in Fig. 7(b) that the d-emission contribution in the actual photoelectron spectra for the ΓAHK plane is not a featureless background, but is a well-defined peak. Bearing in mind the shifts of the p bands proposed in Sec. IV and their possible influence on the shape of the d bands, we cannot rule out the possibility that the calculated bands are incorrect as far as this detailed behavior is concerned. If the calculated bands are correct, however, we have no convincing explanation for this result, and can only offer the following suggestion.

a. Nondirect transitions. Spicer[48] and Doniach[49] have argued that if the optical transition is accompanied by electron scattering, k conservation, in the one-electron sense, will not apply; i.e., it would be possible to observe photoelectrons in the ΓAHK plane, even though there were no initial states in this region of k-space.

b. Surface states. Owing to the shortness of the sampling depth of the photoemission experiment, the bulk band structure may provide only a rough guide to the form of the observed spectra. Emission from surface states has been observed in a number of laboratories.[50,51]

c. Diffuse refraction. If the surface is not perfectly smooth, an electron crossing the boundary may be diffracted such that $\vec{k}_{\parallel}$ is changed by an amount not equal to a reciprocal lattice vector.

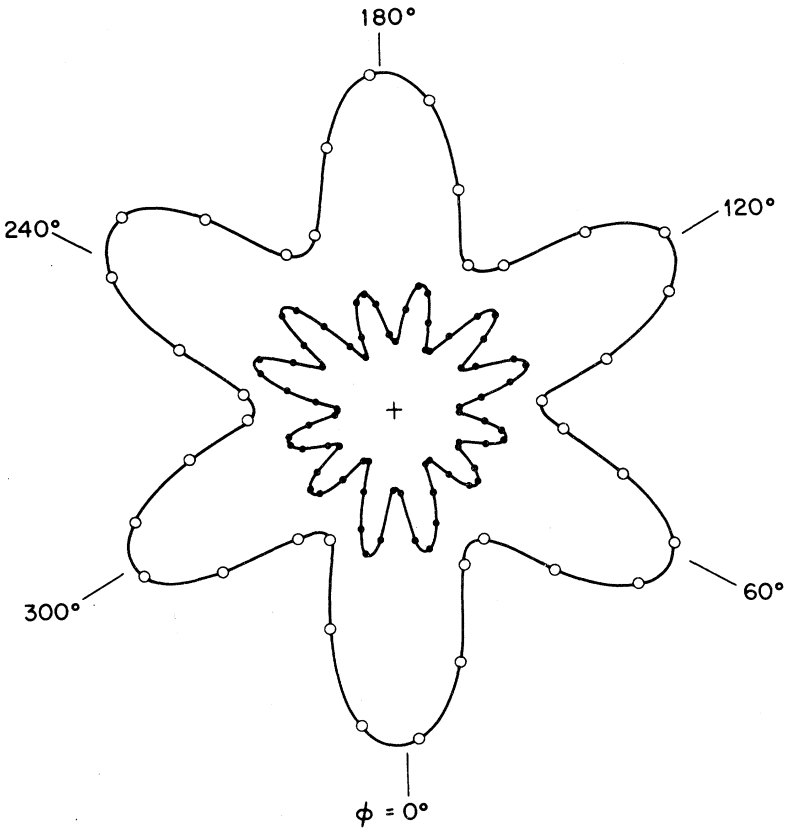

FIG. 21. Radial plots of the azimuthal dependence at $\theta = 55°$ of the total photoemission (open circles) and, on a 10× expanded scale, the d-emission intensity (full circles) from $2H$-$TaSe_2$.

This could result in the appearance of Ta d photoelectrons in the ΓAHK plane.

d. Superlattices. The shorter reciprocal lattice vectors of the superlattice may produce surface-diffraction effects of the kind discussed in c. However, it has been argued in Sec. II A that due to the smallness of the atomic displacements, superlattice effects should be unimportant; i.e., it seems unlikely that the weak diffraction associated with the superlattice could give rise to d emission in the ΓAHK plane whose relative strength is comparable to that in the ΓALM plane. An effect which may be due to the superlattice, and which is in keeping with this requirement of weakness, can be observed in the results for $1T$-$TaSe_2$ shown in Fig. 18. In each pair of major lobes, the lobe at higher ϕ is slightly larger than the other. The consistency of this effect indicates that it is significant. It is observed also in $1T$-TaS_2 but not in $2H$-$TaSe_2$ (see below) which does not form a superlattice at room temperature.

F. Escape depth in $2H$-$TaSe_2$

The ϕ dependence of the Ta d emission has also been measured in the $2H$-polytype of $TaSe_2$, and the results for $\theta = 55°$ are shown in Fig. 21. As in Fig. 15, the outer curve in Fig. 21 represents the total photocurrent. The inner curve represents, on a 10-times-expanded scale, the photocurrent in an energy window which contains the Ta d-emission peak. As expected for the $2H$ polytype, the symmetry of the emission is close to sixfold. However, in the Ta d-emission, we note significant residual threefold symmetry; the pairs of lobes centered at $\phi = 0°$, 120°, and 240° are larger than those centered at 60°, 180°, and 300°. We attribute this lower symmetry to the finite attenuation length of the photoelectrons. The threefold symmetry of the outermost Se-Ta-Se sandwich impresses itself on the observed emission.

Let us assume that the photoemission from the outermost (or first) sandwich and the other odd third, fifth, etc.) sandwiches would look rather like the inner curve of Fig. 15. Let us assume that the even (second, fourth, sixth, etc.) sandwiches produce a similar pattern, but rotated through 180°. In a simple approximation, the observed pattern will be a superposition of the even and odd patterns in the ratio $e^{-d/l}$, where d is the intersandwich spacing (which, for $2H$-$TaSe_2$, equals $c/2 = 6.35$ Å).[52] We find that a reasonable simulation of the d-emission pattern of Fig. 21 can be obtained by superposing two of the d-emission patterns of Fig. 15 in the ratio 0.61:1. This yields an estimate of

$l = 13$ Å for photoelectrons of this particular energy (about 9.4 eV above the Fermi level). This value is comparable to those obtained on other materials by different methods.[53]

The crude analysis presented above assumes that the crystal surface consists of an unstepped cleavage plane. Inspection of the $2H$ structure in Fig. 1 reveals that either of two orientations for the outermost sandwich are possible depending on whether the cleave takes place along the upper face of the unit cell, or along its midplane. We have no estimate of how many steps were present on our sample surface.[54] We note, however, that averaging over multiple steps of both orientations will enhance the sixfold symmetry at the expense of the threefold symmetry. This would lead us to overestimate l, so that the true value may well be smaller than the 13 Å quoted above. We have no knowledge of what the preferred orientation of the outermost Se-Ta-Se sandwich actually was in our experiments.

VI. CONCLUSIONS

It has been found in this series of experiments on layer compounds that angular-resolved photoemission spectroscopy offers a wealth of information not attainable with conventional photoemission techniques. The information derived falls roughly into the following three main categories.

(i) Monitoring the positions of peaks in the photoelectron energy spectra as a function of angle has enabled us to plot empirical $\mathcal{E}(\vec{k})$ dispersion relations which compare favorably with first-principles calculations by Mattheiss.[18] The directness of the method is to be contrasted with other techniques which infer the band structure from some derived quantity such as, the density of states.

(ii) Measurement of the angular dependence of the photoemission intensities appears to be giving information on the properties of the electronic wave functions. It is not yet clear just how much of the observed anisotropy results from the properties of the final states in the optical transitions (as in the recent formalism by Liebsch[43]), and how much is due to initial-state orbitals effects (as in the approach of Gadzuk[44]). If an energy range can be found in which it is reasonable to treat the final state as a plane wave, one has the very appealing result that the photoemission intensity is proportional to the momentum density of the initial-state wave functions. To test this possibility, theoretical calculations of the momentum density would be welcome. There may ultimately be some fruitful connections here with Compton scattering and positron annihilation studies, which also measure some section of the electronic momentum density.

(iii) The surface sensitivity of the photoemission process reveals itself in the observed rotational symmetry of the emission. Symmetry analysis therefore offers a promising way of separating bulk and surface contributions to the spectra in systems where the surface and bulk atoms are arranged with different symmetry.

ACKNOWLEDGMENTS

We are indebted to F. J. DiSalvo for providing the single crystals used in this study, and for his help and encouragement. We have benefitted from valuable communications with J. W. Gadzuk and from discussions with A. Liebsch, E. G. McRae, L. F. Mattheiss, J. C. Phillips, J. E. Rowe, and J. A. Wilson. Thanks are due also to W. E. Black for skillful fabrication of equipment.

[1] E. O. Kane, Phys. Rev. Lett. 12, 97 (1964); G. D. Mahan, Phys. Rev. B 2, 4334 (1970); W. L. Schaich and N. W. Ashcroft, *ibid.* 3, 2452 (1971).
[2] Early work includes that by H. E. Ives, A. R. Olpin, and A. L. Johnsrud, Phys. Rev. 32, 57 (1928); and references therein.
[3] U. Gerhardt and E. Dietz, Phys. Rev. Lett. 26, 1477 (1971).
[4] T. Gustafsson, P. O. Nilsson, and L. Walldén, Phys. Lett. A 37, 121 (1971).
[5] F. Wooten, T. Huen, and H. V. Winsor, Phys. Lett. A 36, 351 (1971).
[6] I. Lindau and S. B. M. Hagstrom, J. Phys. E 4, 936 (1971).
[7] C. S. Fadley and S. A. L. Bergström, in *Electron Spectroscopy*, edited by D. A. Shirley (North-Holland, Amsterdam, 1972), p. 233.
[8] R. Y. Koyama and L. R. Hughey, Phys. Rev. Lett. 29, 1518 (1972).
[9] R. H. Williams, J. M. Thomas, M. Barber, and N. Alford, Chem. Phys. Lett. 17, 142 (1972).
[10] F. Pauty, G. Matula, and P. J. Vernier, Rev. Sci Instrum. 45, 1203 (1974).
[11] B. Feuerbacher and B. Fitton, Phys. Rev. Lett. 30, 923 (1973).
[12] R. T. Poole, R. C. G. Leckey, J. G. Jenkin, and J. Liesegang, J. Electron. Spectrosc. 1, 371 (1973).
[13] N. V. Smith and M. M. Traum, Phys. Rev. Lett. 31, 1247 (1973).
[14] M. M. Traum, N. V. Smith, and F. J. DiSalvo, Phys. Rev. Lett. 32, 1241 (1974).
[15] N. V. Smith, M. M. Traum, and F. J. DiSalvo, Solid State Commun. 15, 211 (1974).
[16] N. V. Smith and M. M. Traum, Surf. Sci. 45, 745 (1974).
[17] J. A. Wilson and A. D. Yoffe, Adv. Phys. 18, 193 (1969); and references therein.
[18] L. F. Mattheiss, Phys. Rev. B 8, 3719 (1973).
[19] H. P. Hughes and W. Y. Liang, J. Phys. C 6, 1684 (1973).
[20] R. H. Williams and A. J. McEvoy, Phys. Status Solidi B 47, 217 (1971).
[21] J. C. McMenamin and W. E. Spicer, Phys. Rev. Lett. 29, 1501 (1972).

[22]P. M. Williams and F. R. Shepherd, J. Phys. C 6, L36 (1973).
[23]G. K. Wertheim, F. J. DiSalvo, and D. N. E. Buchanan, Solid State Commun. 13, 1225 (1973).
[24]R. B. Murray and R. H. Williams, Philos. Mag. 29, 473 (1974); R. H. Williams, J. Phys. C 6, L32 (1973).
[25]R. Huisman and F. Jellinek, J. Less-Common Met. 17, 111 (1969); and references therein.
[26]More precisely, $TaSe_2$ occurs in the $2Ha$ polytype, referred to as just $2H$ in this paper; the $2Hb$ (or MoS_2 structure) has been observed for samples of composition $Ta_{1.10}Se_2$ by R. Huisman, F. Kadijk, and F. Jellinek, J. Less-Common Met. 12, 423 (1967).
[27]E. Bjerklund and A. Kjekshus, Acta Chem. Scand. 21, 513 (1967).
[28]F. J. DiSalvo, R. G. Maines, and J. V. Waszczak, Solid State Commun. 14, 497 (1974).
[29]J. A. Wilson, F. J. DiSalvo, and S. Mahajan, Phys. Rev. Lett. 32, 882 (1974).
[30]R. A. Bromley and R. B. Murray, J. Phys. C. 5, 738 (1972); R. B. Murray, R. A. Bromley, and A. D. Yoffe, *ibid.* 5, 746 (1972); 5, 759 (1972); R. B. Murray and A. D. Yoffe, *ibid.* 5, 3038 (1972).
[31]D. R. Edmondson, Solid State Commun. 10, 1085 (1972).
[32]J. B. Goodenough, Mater. Res. Bull. 3, 409 (1968).
[33]R. Huisman, R. DeJonge, C. Haas, and F. Jellinek, J. Solid State Chem. 3, 56 (1971).
[34]R. V. Kasowski, Phys. Rev. Lett. 30, 1175 (1973).
[35]D. W. Fischer, Phys. Rev. B 8, 3576 (1973).
[36]H. W. Myron and A. J. Freeman, Phys. Rev. 39, 481 (1974).
[37]C. Y. Fong and M. L. Cohen, Phys. Rev. Lett. 32, 720 (1974).
[38]G. F. Derbenwick, Ph.D. thesis, Stanford Electronics Laboratories report, 1970 (unpublished).
[39]L. R. Canfield, G. Haas, and W. R. Hunter, J. Phys. (Paris) 25, 154 (1964).
[40]*International Tables for X-Ray Crystallography*, edited by C. H. MacGillavry, G. D. Rieck and K. Lonsdale (Kynoch, Birmingham, England, 1968), Vol. III, p. 201–216.
[41]S. P. Kowalczyk, L. Ley, F. R. McFeely, R. A. Pollak, and D. A. Shirley, Phys. Rev. B 9, 381 (1974).
[42]D. E. Sayers, F. W. Lytle, and E. A. Stern, in *Advances in X-Ray Analysis*, edited by B. L. Henke, J. B. Newkirk, and G. R. Mallett (Plenum, New York, 1970), Vol 13, p. 248.
[43]A. Liebsch, Phys. Rev. Lett. 32, 1203 (1974).
[44]J. W. Gadzuk, in Proceedings of the Thirty-Second Physical Electronics Conference, Albuquerque, N. M., 1972 (unpublished); J. Vac. Sci. Technol. 11, 274 (1974); Phys. Rev. B 10, 5030 (1974).
[45]We have assumed that the Fermi surface for $1T$-$TaSe_2$ will not differ greatly from that of $1T$-TaS_2 as calculated by Mattheiss (Ref. 18). The experimental results for the Ta d emission at $\theta = 55°$ in $1T$-TaS_2 (see Fig. 17) are very similar indeed to those obtained at $\theta = 55°$ on $1T$-$TaSe_2$ (see Figs. 15 and 16). A band-structure analysis performed for $1T$-TaS_2 differs only in minor details from that for $1T$-$TaSe_2$ in Fig. 18.
[46]B. Podolsky and L. Pauling, Phys. Rev. 34, 109 (1929).
[47]Other orbitals we have considered are the sd^3 hybrids of K. Ganzhorn, Z. Naturforsch. A 7, 291 (1952). The results are qualitatively similar to those in Fig. 19; in particular, they fail to reproduce the bifurcation into pairs of lobes as observed.
[48]W. E. Spicer, Phys. Rev. 154, 385 (1967).
[49]S. Doniach, Phys. Rev. B 2, 3898 (1970).
[50]L. F. Wagner and W. E. Spicer, Phys. Rev. Lett. 28, 1381 (1972).
[51]B. Feuerbacher and B. Fitton, Phys. Rev. Lett. 29, 786 (1972); B. J. Waclawski and E. W. Plummer, Phys. Rev. Lett. 29, 783 (1972).
[52]B. E. Brown and D. J. Beernsten, Acta Cryst. 18, 31 (1965).
[53]C. J. Powell, Surf. Sci. 44, 29 (1974).
[54]B. J. Mrstik and co-workers have seen evidence in low-energy-electron diffraction for steps with areas larger than 1 mm^2 on some air-cleaved samples of $2H$-MoS_2 and $2H$-$NbSe_2$ (private communication).